Communications in Nonlinear Science and Numerical Simulation 116 (2023) 106782

Contents lists available at ScienceDirect

Communications in Nonlinear Science and Numerical Simulation

journal homepage: www.elsevier.com/locate/cnsns

Research paper

Thermal-fluid topology optimization with unconditional energy stability and second-order accuracy via phase-field model

Qing Xia [a], Gangming Sun [a], Qian Yu [a], Junseok Kim [b], Yibao Li [a,*]

[a] School of Mathematics and Statistics, Xi'an Jiaotong University, Xi'an 710049, China
[b] Department of Mathematics, Korea University, Seoul 02841, Republic of Korea

ARTICLE INFO

Article history:
Received 16 May 2022
Received in revised form 24 July 2022
Accepted 29 July 2022
Available online 4 August 2022

Keywords:
Phase-field model
Thermal-fluid topology optimization
Unconditionally energy stability
Fluid–structure interaction
Second-order accurate

ABSTRACT

This paper aims to establish a novel and efficient topology optimization method for the thermal-fluid. To adaptively design the fluid–solid coupling structure and make the objective energy to dissipate, the proposed method considers several constraints, such as the volume conservation, inlet and outlet flow velocity field and fluid–solid boundary constraints. The governing system includes the phase-field model, the steady state Darcy equation and the heat transfer equation. Under the constraints of multiple physical fields, we prove the existence of minimal solutions to the optimization problem. We use a Crank–Nicolson (CN) type scheme to discretize the governing system. The multigrid method is used to solve the resulting system of discrete equations. We prove the boundedness and unconditional stability of the original energy, which implies that a large time step can be used. The proposed discrete system is both spatially and temporally second-order accurate. Various computational tests have been performed to demonstrate that the numerical approach is efficient in designing the complicated structures of thermal fluid flows.

1. Introduction

Topology optimization [1–5] has been attracting considerable interest in various physical processes, such as shape optimization of transport vehicles [6,7], optimal pipe bending structure [8,9] and biomechanical production of artificial stents [10,11]. Thermal-fluid topology optimization considers the influence of the fluid flow to design the composite structure under the limitation of physical constraints, which has gained extensive attention in thermal engineering applications [12], such as gas turbine production [13], heat sink device production [14] and 3D printing [15,16]. The topology optimization of thermal-fluid system in literature can be classified into the following categories: the motion of fluid flow, the heat conduction and convection and the coupled thermal-fluid problems. Borrvall and Petersson [17] introduced an objective energy with a Brinkman penalization sink term for the momentum equation. By minimizing the dissipated energy in the fluid, the optimized shape can be obtained. Various extended works such as studies with incompressible Navier–Stokes flows [18,19], no-slope-selection thin film and gradient models [20], laminar flows with minimized pressure drop [21,22], Darcy flows with maximized flow uniformity at the outlet [23,24], have been conducted

* Corresponding author.
E-mail address: yibaoli@xjtu.edu.cn (Y. Li).
URL: http://gr.xjtu.edu.cn/web/yibaoli (Y. Li).

https://doi.org/10.1016/j.cnsns.2022.106782
1007-5704/

in the last decade. The topology optimization of heat conduction and convection, which involved variation of temperature between fluid and solid domain based on the thermal interactions, has been proved to offer the optimal structures with unconventional tree-like shape [25,26]. The studies on the thermal-fluid system coupled with the two categories have been implemented after the wide applications of the topology optimizations for the heat conduction and fluid flow [27,28].

Topology optimization was originally based on the homogenization theory [29] and now evolved into different directions, which can be roughly categorized as: density approach, evolutionary approaches, topological derivative, level-set method and phase-field method. Sigmund and Clausen [30] used the mixed displacement–pressure formulation to solve the pressure load problem of the topology optimization based on the standard density approach. This method defined the void phase as a hydrostatic incompressible fluid to transfer the pressure from the external boundary to the internal structure, which was independent of the shape or topology. Motivated by this method, various density-based schemes were proposed for the applications of the large scale Stokes flow problems [31], turbulent flows problems [32] and steady-state fluid–structure interaction problem [33]. Vicente et al. [34] carried out the finite element analysis for the frequency response of a multiphysics system involving fluid–structure interaction. They applied the bi-directional evolutionary structural optimization approach to circumvent the problems faced by the density based optimization methods, in which the acoustic structure interfaces can change their locations during the optimization process. The evolutionary method has been widely studied in recent years [35–37]. The topological derivative-based method was applied to design the fluid flow channel where solid and fluid material was distributed in a porous medium [38–40]. Challis and Guest [41] used the level-set method for the optimization in Stokes flow. Kreissl and Maute [42] discretized the topology optimization system by the extended finite element method and used a level-set method to describe the fluid-solid interface geometry. Additionally, the level-set equation was needed to be reset in the middle of computation to ensure the continuous update of the governing partial differential equation (PDE) so that the convergence rate of the optimization program decreases [43]. To overcome these problems, the phase-field method [44,45] has been a recently emerged approach within the field of topology optimization. Garcke et al. [46] considered the phase field based topology optimization problems and distributed some mathematically profound work [47,48], which is concerned with the well-posedness, existence, convergence study of the phase field based system for solving topological optimization problems. A considerable amount of work based on phase field model further extended its theoretical and numerical research of topology optimization [49,50]. Furthermore, quite a few existing works of convergence analysis [51,52] and error estimate [53] for the phase field model coupled with fluid motion were performed to verify the superiority of the phase field method.

In this paper, we will establish an efficient topology optimization system for the thermal-fluid. The computational framework is coupled with the time-dependent Allen–Cahn (AC) equation, the incompressible Stokes equation and the heat transfer (HT) equation, which can be used to simulate the evolution of the interfaces in fluid–solid coupling system. Theoretically we prove the existence of the minimum solution of the optimization problem. The governing system has been discretized by the Crank–Nicolson (CN) method to have the second-order temporal accuracy. Furthermore, the Picard-iteration method has been applied for the coupled system. The resulting system can be proved to be unconditionally energy stable. Several numerical tests will be performed to verify the robust performance of the proposed method.

The contents of this paper are as follows: In Section 2, we briefly introduce the constrained thermodynamic topology optimization problem. In Section 3, we provide the detailed description of the proposed Crank–Nicolson-type scheme with second-order temporal accuracy and prove the unconditional energy stability of the numerical system. Section 4 is devoted to present various computation tests. Concluding remarks are given in Section 5.

2. Formulation of topology optimization problems

In this section, we introduce the shape optimization problem with thermal-fluid based on a phase-field model. Using the constraints of the incompressible Stokes equation and convective heat transfer equation, the ultimate optimal shape can be obtained by the proposed topology optimization scheme.

2.1. The description of original optimization problems

We first introduce the original optimization problem by minimizing a certain objective functional with the constraints of incompressible Stokes equation and convective HT equation. The optimized shapes and fluid-solid domain can be chosen in a given, fixed Lipschitz domain $\Omega \subseteq \mathcal{R}^m (m = 2, 3)$. Let $\partial\Omega$ denote its boundary and the outer normal vector for Ω is denoted by $\mathbf{n}$. Let us introduce $\phi \in L^1(\Omega)$ as a characteristic function of bounded variation in Ω and denote $V(\Omega, \{0, 1\})$ as the space of functions of bounded variation in Ω, which can be interpreted as $\phi = 1(\mathbf{x} \in \Omega_f)$ and $\phi = 0(\mathbf{x} \in \Omega_s)$. By introduce the Caccioppoli set $E \subset \Omega$ with $\phi := \chi_E \in V(\Omega, \{0, 1\})$, we can use the corresponding Caccipppoli set $\Omega_f := \{\phi = 1\}$ to define the fluid subdomain. Furthermore, we denote the solid subdomain as $\Omega_s = \Omega \backslash \Omega_f$. The original model for shape optimization can be defined as the minimization of the following functional:

$$\min_{\Omega} J_{\text{ori}}(\mathbf{u}, T) = \int_{\Omega_f} \left(\frac{\mu}{2} |\nabla \mathbf{u}|^2 - \mathbf{u} \cdot \mathbf{f} \right) \mathrm{d}\mathbf{x} + \int_{\Omega} \frac{1}{2} T^2 \mathrm{d}\mathbf{x} + \gamma \Gamma(\Omega_f), \tag{1}$$

subject to

$$\begin{cases} \nabla p - \nabla \cdot (\mu \nabla \mathbf{u}) = \mathbf{f} & \text{in } \Omega_f, \\ \nabla \cdot \mathbf{u} = 0 & \text{in } \Omega_f, \\ \mathbf{n} \cdot \nabla p = 0 & \text{on } \partial\Omega_f, \\ \mathbf{u} = \mathbf{0} & \text{in } \Omega_s, \\ \nabla \mathbf{u} \cdot \mathbf{n} = 0 & \text{on } \partial\Omega_f, \\ \mathbf{u} = \mathbf{g} & \text{on } \partial\Omega_s, \end{cases} \tag{2}$$

$$\begin{cases} \rho C_p T_t = \nabla \cdot (K \nabla T) - \rho C_p \mathbf{u} \cdot \nabla T & \text{in } \Omega, \\ \nabla T \cdot \mathbf{n} = 0 & \text{on } \partial\Omega. \end{cases} \tag{3}$$

The objective functional of the fluid topology optimization Eq. (1) is composed of the following parts: The first term is the compliance energy for the Stokes flow, where μ is the viscosity of the fluid, $\mathbf{u}$ is the velocity field and $\mathbf{f}$ is the external force act on the whole of Ω. The second term is the thermal energy, where T is the temperature field. The last term is the perimeter penalization, where γ is the positive penalized parameter and $\Gamma(\Omega_f)$ is the length of the perimeter of Ω_f. This term is added to overcome the issue of lacking the general existence of minimizer [54]. The notations for the constrained conditions are denoted as follows: p is the pressure field of the fluid. K, C_p and ρ is the thermal conductivity coefficient, the thermal capacity and density of the fluid, respectively. It should be emphasized that the velocity field is defined on the whole of Ω, while in Ω_f it is constrained by the Stokes functional and in Ω_s we set $\mathbf{u} = \mathbf{0}$.

2.2. The objective functional of the shape optimization problem based on the phase-field model

In this subsection, we will modify the objective functional based on the phase-field model. The non-fluid region has been replaced by a porous medium with small permeability [17], which implies that we can extend the fluid computing region(Ω_f) into full the whole computational(Ω). The sharp interface between the solid region(low permeability fluid) and the fluid region has been replaced by a diffuse interface. The design variable used to distinguish the regions filled or not filled with fluid is denoted by ϕ, which is chosen in $H^1(\Omega)$. We take different values to represent the fluid domain($\phi = 1$) and solid domain($\phi = 0$), respectively. The diffuse interface between fluid and solid denoted by $|\phi| \leq 1$. To replace the multiple of perimeter functional $\gamma\Gamma(\Omega_f)$ in the original objective functional Eq. (1), we use the multiple of Ginzburg–Landau energy [55]

$$\gamma E(\phi) = \gamma \int_\Omega \left(\frac{\epsilon}{2} |\nabla \phi|^2 + \frac{1}{\epsilon} F(\phi) \right) d\mathbf{x} \tag{4}$$

where $F(\phi) = \phi^2(1-\phi)^2/4$ is the double well potential. Here γ is considered as the weighting parameter of the approximation substitution, which forces Eq. (4) to converge as $\epsilon \to 0$. The two constrains are equivalent since the Ginzburg–Landau energy is the approximation of the perimeter functional refer to [56]. Here ϵ is proportional to the interfacial thickness and ∇ denotes the gradient operator of the computation. Considering that we substitute porous medium for solid domain, the permeability $\alpha_\epsilon(\phi) : [0, 1] \to [0, \tilde{\alpha}_\epsilon]$ is defined as a smooth function of ϕ and the stokes flow is transformed to Darcy flow as:

$$\alpha_\epsilon(\phi)\mathbf{u} - \nabla \cdot (\mu \nabla \mathbf{u}) = \mathbf{u} \tag{5}$$

where $\alpha_\epsilon(\phi)$ is decreasing, surjective and continuous for ϵ. In this paper, we chose $\alpha_\epsilon(\phi) = \tilde{\alpha}_\epsilon (1-\phi)$, which is introduced for hydrodynamic topology optimization in [57]. Here $(\tilde{\alpha}_\epsilon)^{-1}$ is the permeability and satisfy $\tilde{\alpha}_\epsilon \geq 0$. Considering the smoothness and well-determined of the porous medium system, we impose that $\lim_{\epsilon \to 0} \tilde{\alpha}_\epsilon < \infty$ and $\tilde{\alpha}_\varepsilon = o\left(\varepsilon^{-\frac{2}{3}}\right)$. Thus, a penalty term $\int_\Omega \alpha_\epsilon(\phi)|\mathbf{u}|^2/2 d\mathbf{x}$ is added to the modified energy, which confirm that the velocity is small enough in the porous medium(i.e., $\phi = 0$) and satisfies $\lim_{\epsilon \to 0} \mathbf{u} = \mathbf{0}$. In addition, a volume constrain has be considered in the modified objective functional to yield an upper bound on the amount of fluid. We use $V(\phi) := \int_\Omega \phi d\mathbf{x}$ to denote the volume of the region fulfilling fluid and add the penalty term $\beta (V(\phi) - V_0)^2 /2$ to the modified objective functional, where V_0 is the desired volume. Here β is a positive parameter, which limits the influence of the volume constraint and can be chosen corresponding to the application. As discussed above, the modified objective function can be summarized as:

$$\begin{aligned} \min_\Omega J(\phi, \mathbf{u}, T) = & \int_\Omega \left(\frac{\mu}{2} |\nabla \mathbf{u}|^2 - \mathbf{u} \cdot \mathbf{f} \right) d\mathbf{x} + \gamma \int_\Omega \left(\frac{\epsilon}{2} |\nabla \phi|^2 + \frac{1}{\epsilon} F(\phi) \right) d\mathbf{x} \\ & + \int_\Omega \frac{\alpha(\phi)}{2} |\mathbf{u}|^2 d\mathbf{x} + \int_\Omega \frac{1}{2} T^2 d\mathbf{x} + \frac{\beta}{2} \left(\int_\Omega \phi d\mathbf{x} - V_0 \right)^2 \end{aligned} \tag{6}$$

subject to

$$\begin{cases} \nabla p - \nabla \cdot (\mu \nabla \mathbf{u}) + \alpha_\epsilon(\phi)\mathbf{u} = \mathbf{f} & \text{in } \Omega, \\ \nabla \cdot \mathbf{u} = 0 & \text{in } \Omega, \\ \nabla \mathbf{u} \cdot \mathbf{n} = 0 & \text{on } \partial\Omega, \\ \mathbf{n} \cdot \nabla p = 0 & \text{on } \partial\Omega. \end{cases} \tag{7}$$

$$\begin{cases} \rho C_p T_t - \nabla \cdot (K \nabla T) + \rho C_p \mathbf{u} \cdot \nabla T = 0 & \text{in } \Omega, \\ \nabla T \cdot \mathbf{n} = 0 & \text{on } \partial\Omega. \end{cases} \tag{8}$$

Some notations should be remarked here: (i) As we replace solid region with porous medium, solid–liquid distinction is no longer considered in the entire computational domain(i.e., $\Omega_s = \emptyset$, $\Omega_f = \Omega$), and the original problem has been converted to a constrained optimization problem of two phase fluids. (ii) The parameters μ, K, ρ and C_p are related to the phase field function, which can be updated by

$$\begin{aligned} \mu(\phi) &= \mu_1 + (\mu_2 - \mu_1)\,\phi, \quad K(\phi) = K_1 + (K_2 - K_1)\,\phi, \\ \rho(\phi) &= \rho_1 + (\rho_2 - \rho_1)\,\phi, \quad C_p(\phi) = C_1 + (C_2 - C_1)\,\phi \end{aligned} \tag{9}$$

where μ_i, K_i, ρ_i and C_i(i=1,2) denotes the constant viscosity, thermal conductivities, density and thermal capacity of the two phases, respectively. Additionally, we assume that μ_i, K_i, ρ_i and C_i are all temperature independent.

Based on the variational derivation, we apply the gradient flow approach. The evolution of the phase-field function $\phi(\mathbf{x}, t)$ is governed by:

$$\frac{\partial \phi}{\partial t} = -\frac{\delta J}{\delta \phi} = -\frac{\gamma}{\epsilon} F'(\phi) + \gamma \epsilon \Delta \phi - \frac{\alpha'_\epsilon(\phi)}{2} |\mathbf{u}|^2 - \beta\,(V(\phi) - V_0) \tag{10}$$

using the following variational principle of the objective functional:

$$\begin{aligned} &\left(\frac{\delta J}{\delta \phi}, \psi\right)_{L_2} = \frac{\mathrm{d}}{\mathrm{d}\eta} J(\phi + \eta\psi, \mathbf{u}, T)\Big|_{\eta=0} \\ &= \frac{\gamma}{\epsilon} \int_\Omega \left(\psi F'(\phi) + \epsilon^2 \nabla\psi \cdot \nabla\phi\right) \mathrm{d}\mathbf{x} + \int_\Omega \psi \left(\frac{\alpha'_\epsilon(\phi)}{2} |\mathbf{u}|^2 + \beta\,(V(\phi) - V_0)\,V'(\phi)\right) \mathrm{d}\mathbf{x} \\ &= \frac{\gamma}{\epsilon} \int_\Omega \left(F'(\phi) - \epsilon^2 \Delta\phi\right) \psi \,\mathrm{d}\mathbf{x} + \int_\Omega \psi \left(\frac{\alpha'_\epsilon(\phi)}{2} |\mathbf{u}|^2 + \beta\,(V(\phi) - V_0)\,V'(\phi)\right) \mathrm{d}\mathbf{x} + \gamma \int_{\partial\Omega} \epsilon^2 \frac{\partial \phi}{\partial n} \psi \,\mathrm{d}s \\ &= \int_\Omega \left(\frac{\gamma}{\epsilon} F'(\phi) - \frac{\gamma}{\epsilon} \epsilon^2 \Delta\phi + \frac{\alpha'_\epsilon(\phi)}{2} |\mathbf{u}|^2 + \beta\,(V(\phi) - V_0)\,V'(\phi)\right) \psi \,\mathrm{d}\mathbf{x}, \end{aligned}$$

where we use the Neumann boundary condition for the phase variable, i.e., $\nabla\phi \cdot \mathbf{n} = 0$ and $(\cdot)_{L_2}$ is the L_2 norm inner product. Furthermore, we can obtain the derivation of the proposed equation of the velocity $\mathbf{u}$ in the similar way:

$$\begin{aligned} &\left(\frac{\delta J}{\delta \mathbf{u}}, \mathbf{v}\right)_{L_2} = \frac{\mathrm{d}}{\mathrm{d}\eta} J(\phi, \mathbf{u} + \eta\mathbf{v}, T)\Big|_{\eta=0} \\ &= \int_\Omega (\mu \nabla\mathbf{u} \cdot \nabla\mathbf{v}) \mathrm{d}\mathbf{x} - \int_\Omega \mathbf{f} \cdot \mathbf{v} \mathrm{d}\mathbf{x} + \int_\Omega \alpha_\epsilon(\phi)\mathbf{u} \cdot \mathbf{v} \mathrm{d}\mathbf{x} - \int_\Omega p \nabla \cdot \mathbf{v} \mathrm{d}\mathbf{x} - \int_{\partial\Omega} \mathbf{n} \cdot \nabla p \mathrm{d}s \\ &= \int_\Omega \left(\nabla p - \nabla \cdot (\mu \nabla \mathbf{u}) - \int_\Omega \mathbf{f} \mathrm{d}\mathbf{x} + \alpha_\epsilon(\phi)\mathbf{u}\right) \mathbf{v} \mathrm{d}\mathbf{x}, \end{aligned} \tag{11}$$

which subjects to

$$\frac{\delta J}{\delta \mathbf{u}} = \nabla p - \nabla \cdot (\mu \nabla \mathbf{u}) + \alpha_\epsilon(\phi)\mathbf{u} - \mathbf{f}. \tag{12}$$

Herein, we have established the hydrodynamic topology optimization system based on the phase field model. In the following parts, we will introduce two significant results with the proposed system.

Theorem 1. *There exists a minimizer* $(\mathbf{x}^*, \phi^*, \mathbf{u}^*, T^*)$ *to the optimization problem Eq. (6) with the constrains Eqs. (7)–(8), i.e.,*

$$\exists (\mathbf{x}^*, \phi^*, \mathbf{u}^*, T^*) \in \Omega \times \Phi \times U \times T_s, \quad s.t.\ J(\mathbf{x}^*, \phi^*, \mathbf{u}^*, T^*) \le J(\mathbf{x}, \phi, \mathbf{u}, T), \tag{13}$$

where ϕ *belongs to* $\Phi \subset \mathcal{R}^d$, $\mathbf{u}$ *belongs to* $\mathbf{U} \subset \mathcal{R}^{d\times d}$ *and* T *belongs to* $T_s \subset \mathcal{R}^d$. *Here* $\mathbf{U}$, Φ *and* T_s *are closed and weakly closed of* $H^1(\Omega)$.

Proof. Without loss of generality, we assume $J(\mathbf{x}, \phi, \mathbf{u}, T) : (\Omega, \Phi, U, T_s) \rightarrow \mathcal{R}$ satisfies the Carathéodory condition, which can be summarized as

- $J(\mathbf{x}, \cdot, \cdot, \cdot) : \mathcal{R} \times \mathcal{R}^{d\times d} \times \mathcal{R} \rightarrow \mathcal{R}$ is continuous for almost every $\mathbf{x} \in \Omega$.
- $J(\cdot, \phi, \mathbf{u}, T) : \Omega \rightarrow \mathcal{R}$ is Lebesgue-measurable for each $\phi \in \mathcal{R}^d$, $\mathbf{u} \in \mathcal{R}^{d\times d}$ and $T \in \mathcal{R}^d$.

Based on the Carathéodory existence theorem, we derive that J has a constant lower bound. Refer to [54], the solution $\mathbf{u}$ and T are measurable and bounded. Thus we can define a solution operator as

$$\begin{aligned} &S : \Phi \rightarrow \mathbf{U} \ \text{ and } \ S(\phi) := \mathbf{u}, \ \text{ such that } \mathbf{u} \text{ satisfies the constrain Eq. (7).} \\ &G : \Phi \rightarrow \mathbf{T_s} \ \text{ and } \ G(\mathbf{u}) := T, \ \text{ such that } T \text{ satisfies the constrain Eq. (8).} \end{aligned} \tag{14}$$

Let us choose an admissible sequence $\lim_{i\rightarrow+\infty}(\phi_i, \mathbf{u}_i, T_i)_{i\in\mathcal{N}} \rightarrow (\phi_0, \mathbf{u}_0, T_0) \subset \Phi \times \mathbf{U} \times T_s$, particularly, the sequence satisfies $\mathbf{u}_i = S(\phi_i)$ and $T_i = G(\mathbf{u}_i)$ for all $i \in \mathcal{N}$. Then we will prove in turn that (i) $(\phi_0, \mathbf{u}_0, T_0)$ is admissible of Eqs. (6)–(8) and (ii) the optimization problem J satisfies the weak lower semicontinuous property.

(i) For the fixed $\mathbf{v} \in \mathbf{U}$, we can obtain that

$$\begin{aligned} &\lim_{i\rightarrow+\infty} \int_\Omega \left(\alpha_\epsilon\left(\phi_i\right)\boldsymbol{u}_i - \alpha_\epsilon\left(\phi_0\right)\boldsymbol{u}_0\right)\cdot\mathbf{v}\mathrm{d}\mathbf{x} \\ &= \int_\Omega \left(\alpha_\epsilon\left(\phi_i\right)\mathbf{u}_i - \alpha_\epsilon\left(\phi_i\right)\mathbf{u}_0\right)\cdot\mathbf{v}\mathrm{d}\mathbf{x} + \int_\Omega \left(\alpha_\epsilon\left(\phi_i\right)\mathbf{u}_0 - \alpha_\epsilon\left(\phi_0\right)\mathbf{u}_0\right)\cdot\mathbf{v}\mathrm{d}\mathbf{x} = 0, \end{aligned}$$

since that

$$\begin{cases} \displaystyle\int_\Omega \left(\alpha_\epsilon\left(\phi_i\right)\mathbf{u}_i - \alpha_\epsilon\left(\phi_i\right)\mathbf{u}_0\right)\cdot\mathbf{v}\mathrm{d}\mathbf{x} \le \tilde{\alpha}_\epsilon \left\|\mathbf{u}_i - \mathbf{u}_0\right\|_{L^2(\Omega)} \|\mathbf{v}\|_{L^2(\Omega)} \text{ and } \lim_{i\rightarrow+\infty} \left\|\mathbf{u}_i - \mathbf{u}_0\right\|_{L^2(\Omega)} = 0, \\ \displaystyle\lim_{i\rightarrow+\infty} \int_\Omega \left(\alpha_\epsilon\left(\phi_i\right)\mathbf{u}_0 - \alpha_\epsilon\left(\phi_0\right)\mathbf{u}_0\right)\cdot\mathbf{v}\mathrm{d}\mathbf{x} = \lim_{i\rightarrow+\infty} \int_\Omega \left(\alpha_\epsilon\left(\phi_i\right) - \alpha_\epsilon\left(\phi_0\right)\right)\left(\mathbf{u}_0\cdot\mathbf{v}\right)\mathrm{d}\mathbf{x} = 0. \end{cases}$$

Refer to [58], there exists pressure $p \in L^2(\Omega)$ such that $\mathbf{u}_0 = S(\phi_0)$ and $T_0 = G(\mathbf{u}_0)$.

(ii) According to the Cauchy sequences of sequence of functions, we obtain that

$$\begin{aligned} &\lim_{i\rightarrow+\infty} \int_\Omega F\left(\phi_i\right)\mathrm{d}\mathbf{x} = \int_\Omega F\left(\phi_0\right)\mathrm{d}\mathbf{x}, \\ &\lim_{i\rightarrow+\infty} \int_\Omega |\nabla\mathbf{u}_i|^2\mathrm{d}\mathbf{x} = \int_\Omega |\nabla\mathbf{u}_0|^2\mathrm{d}\mathbf{x}, \\ &\lim_{i\rightarrow+\infty} \int_\Omega |\nabla\phi_i|^2\mathrm{d}\mathbf{x} = \int_\Omega |\nabla\phi_0|^2\mathrm{d}\mathbf{x}. \\ &\lim_{i\rightarrow+\infty} \int_\Omega (T_i^2 - T_0^2)\mathrm{d}\mathbf{x} = \lim_{i\rightarrow+\infty} \int_\Omega (T_i + T_0)(T_i - T_0)\mathrm{d}\mathbf{x} \le 2T_{max}\|T_i - T_0\|_{L^2(\Omega)}, \\ &\text{where } \lim_{i\rightarrow+\infty} \|T_i - T_0\|_{L^2(\Omega)} = 0 \ \text{ and } T_i \text{ is bounded by } T_{max}. \end{aligned} \tag{15}$$

Therefore, we only need to consider the continuous properties of the strongly coupled term in the objective equation.

$$\begin{aligned} &\lim_{i\rightarrow+\infty} \int_\Omega \alpha_\epsilon\left(\phi_i\right)\left|\mathbf{u}_i\right|^2 \ \mathrm{d}\mathbf{x} - \int_\Omega \alpha_\epsilon\left(\phi_0\right)\left|\mathbf{u}_0\right|^2 \ \mathrm{d}\mathbf{x} \\ &= \lim_{i\rightarrow+\infty} \int_\Omega \alpha_\epsilon\left(\phi_i\right)\left(\left|\mathbf{u}_i\right|^2 - \left|\mathbf{u}_0\right|^2\right)\mathrm{d}\mathbf{x} + \lim_{i\rightarrow+\infty} \int_\Omega \left(\alpha_\epsilon\left(\phi_i\right) - \alpha_\epsilon\left(\phi_0\right)\right)\left|\mathbf{u}_0\right|^2 \ \mathrm{d}\mathbf{x} \\ &\le \lim_{i\rightarrow+\infty} \tilde{\alpha}_\epsilon \int_\Omega \left|\mathbf{u}_i - \mathbf{u}_0\right|\left|\mathbf{u}_i + \mathbf{u}_0\right|\mathrm{d}\mathbf{x} + \lim_{i\rightarrow+\infty} \int_\Omega \left(\alpha_\epsilon\left(\phi_i\right) - \alpha_\epsilon\left(\phi_0\right)\right)\left|\mathbf{u}_0\right|^2 \ \mathrm{d}\mathbf{x} \\ &\le \lim_{i\rightarrow+\infty} \tilde{\alpha}_\epsilon \left\|\mathbf{u}_i + \mathbf{u}_0\right\|_{L^2(\Omega)} \left\|\mathbf{u}_i - \mathbf{u}_0\right\|_{L^2(\Omega)} + \lim_{i\rightarrow+\infty} \int_\Omega \left(\alpha_\epsilon\left(\phi_i\right) - \alpha_\epsilon\left(\phi_0\right)\right)\left|\mathbf{u}_0\right|^2 \ \mathrm{d}\mathbf{x} = 0. \end{aligned} \tag{16}$$

The combination of Eqs. (15) and Eq. (16) estimates that the objective function of Eq. (6) is lower semicontinuous, i.e., $J(\phi_0, \mathbf{u}_0, T_0) \le \liminf_{i\rightarrow+\infty} J(\phi_i, \mathbf{u}_i, T_i)$.

Considering the well-posedness of this system and the lower semi-continuity of the objective function, there are at least one minimizer $(\phi_0, \mathbf{u}_0, T_0)$ minimize the objective function J. □

Theorem 2. *Considering the state functions Eqs. (7) and (8), the solution to the system Eq. (10) forces the modified energy Eq. (6) to satisfy the following energy law:*

$$\frac{\mathrm{d}}{\mathrm{d}t}J(\phi,\mathbf{u},T)\le 0,\quad t\ge 0. \tag{17}$$

Proof. By taking the inner product of Eq. (7) with $\mathbf{u}$, Eq. (10) with $-\phi$, and Eq. (8) with T, we can obtain the following energy dissipation law:

$$\begin{aligned}
&\frac{\mathrm{d}}{\mathrm{d}t}J(\phi,\mathbf{u},T)\\
&=\int_\Omega(\mu\nabla\mathbf{u}\cdot\nabla\mathbf{u}_t-\mathbf{f}\cdot\mathbf{u}_t)\,\mathrm{d}\mathbf{x}+\gamma\int_\Omega\left(\epsilon\nabla\phi\cdot\nabla\phi_t+\frac{1}{\epsilon}F'(\phi)\phi_t\right)\mathrm{d}\mathbf{x}\\
&\quad+\int_\Omega\left(\alpha_\epsilon(\phi)\mathbf{u}\cdot\mathbf{u}_t+\frac{\alpha_\epsilon'(\phi)}{2}|\mathbf{u}|^2\phi_t\right)\mathrm{d}\mathbf{x}+\int_\Omega TT_t\mathrm{d}\mathbf{x}+\int_\Omega\beta\left(V(\phi)-V_0\right)V'(\phi)\phi_t\mathrm{d}\mathbf{x}\\
&=\int_\Omega(-\nabla\cdot(\mu\nabla\mathbf{u})\cdot\mathbf{u}_t-\mathbf{f}\cdot\mathbf{u}_t+\alpha_\epsilon(\phi)\mathbf{u}\cdot\mathbf{u}_t)+\int_\Omega TT_t\mathrm{d}\mathbf{x}\\
&\quad+\left(\gamma\int_\Omega-\epsilon\Delta\phi\cdot\phi_t+\frac{1}{\epsilon}F'(\phi)\phi_t+\frac{\alpha_\epsilon'(\phi)}{2}|\mathbf{u}|^2\phi_t+\beta\left(V(\phi)-V_0\right)V'(\phi)\phi_t\right)\mathrm{d}\mathbf{x}\\
&=\int_\Omega-\nabla p\cdot\mathbf{u}_t\mathrm{d}\mathbf{x}-\int_\Omega\phi_t^2\mathrm{d}\mathbf{x}+\frac{1}{\rho C_p}\int_\Omega T\nabla\cdot(K\nabla T)-\rho C_pKT\mathbf{u}\cdot\nabla T\mathrm{d}\mathbf{x}\\
&=-\int_\Omega\phi_t^2\mathrm{d}\mathbf{x}-\int_\Omega\frac{K}{\rho C_p}|\nabla T|^2\mathrm{d}\mathbf{x}\le 0,
\end{aligned}$$

where we have used the following equations:

$$\int_\Omega-\nabla p\cdot\mathbf{u}_t\mathrm{d}\mathbf{x}=\int_\Omega p\nabla\cdot\mathbf{u}_t\mathrm{d}\mathbf{x}-\int_{\partial\Omega}p\mathbf{u}_t\cdot\mathbf{n}\mathrm{d}\mathbf{x}=-\int_{\partial\Omega}p\mathbf{u}_t\cdot\mathbf{n}\mathrm{d}\mathbf{x}=0.$$

This completes the proof. □

3. Numerical scheme for the shape optimization problem

Let us introduce the discrete formulation and implementation for the proposed shape optimization problem. The thermodynamic scheme for topology optimization is discretized in two-dimension domain $\Omega=[a,b]\times[c,d]$ with a $N_x\times N_y$ mesh grid, where N_x and N_y are even integers and $N=N_xN_y$. Then, we denote $h=(b-a)/N_x=(d-c)/N_y$ as the spatial step. Let us consider the following sets: $E_m:=\{i\cdot h\mid i=0,\dots,m\}$, $C_m:=\{(i-1/2)\cdot h\mid i=1,\dots,m\}$ and $C_{\bar m}:=\{(i-1/2)\cdot h\mid i=0,\dots,m+1\}$. Then we have the following function spaces:

$$\begin{aligned}
&\mathcal{C}_{m\times n}=\{\phi:C_m\times C_n\to\mathbf{R}\},\quad \mathcal{C}_{\bar m\times\bar n}=\{\phi:C_{\bar m}\times C_{\bar n}\to\mathbf{R}\},\\
&\mathcal{C}_{\bar m\times n}=\{\phi:C_{\bar m}\times C_n\to\mathbf{R}\},\quad \mathcal{C}_{m\times\bar n}=\{\phi:C_m\times C_{\bar n}\to\mathbf{R}\},\\
&\mathcal{E}^{\mathrm{ew}}_{m\times n}=\{f:E_m\times C_n\to\mathbf{R}\},\quad \mathcal{E}^{\mathrm{ns}}_{m\times n}=\{f:C_m\times E_n\to\mathbf{R}\}.
\end{aligned}\tag{18}$$

The staggered marker-and-cell (MAC) mesh is used in which the pressure and indicator function are stored at cell centers and velocities at cell interfaces. Let us use $\phi^n_{i,j}$, $\mathbf{u}^n_{i,j}$, $p^n_{i,j}$ and $T^n_{i,j}$ to denote the approximation of $\phi(\mathbf{x}_{ij},n\Delta t)$, $\mathbf{u}(\mathbf{x}_{ij},n\Delta t)$, $p(\mathbf{x}_{ij},n\Delta t)$ and $T(\mathbf{x}_{ij},n\Delta t)$, respectively, where Δt is the temporal step. Let us denote the x-dimension and y-dimension center-to-edge average operator as $A_x:\mathcal{C}_{\bar m\times n}\to\mathcal{E}^{\mathrm{ew}}_{m\times n}$ and $A_y:\mathcal{C}_{m\times\bar n}\to\mathcal{E}^{\mathrm{ns}}_{m\times n}$, denote the x-dimension and y-dimension central difference operators as $D_x:\mathcal{C}_{\bar m\times n}\to\mathcal{E}^{\mathrm{ew}}_{m\times n}$ and $D_y:\mathcal{C}_{m\times\bar n}\to\mathcal{E}^{\mathrm{ns}}_{m\times n}$, denote the edge-to-center difference operators as $d_x:\mathcal{E}^{\mathrm{ew}}_{m\times n}\to\mathcal{C}_{m\times n}$ and $d_y:\mathcal{E}^{\mathrm{ns}}_{m\times n}\to\mathcal{C}_{m\times n}$, respectively. Thus we can define the discrete operators before presenting the second-order numerical scheme.

$$\begin{aligned}
&A_x\phi_{i+1/2,j}=\frac{1}{2}\left(\phi_{i,j}+\phi_{i+1,j}\right),\quad D_x\phi_{i+1/2,j}=\frac{1}{h}\left(\phi_{i+1,j}-\phi_{i,j}\right),\\
&A_y\phi_{i,j+1/2}=\frac{1}{2}\left(\phi_{i,j}+\phi_{i,j+1}\right),\quad D_y\phi_{i,j+1/2}=\frac{1}{h}\left(\phi_{i,j+1}-\phi_{i,j}\right),\\
&d_x\phi_{i,j}=\frac{1}{h}\left(\phi_{i+1/2,j}-\phi_{i-1/2,j}\right),\quad d_y\phi_{i,j}=\frac{1}{h}\left(\phi_{i,j+1/2}-\phi_{i,j-1/2}\right),\\
&\Delta_d\phi_{i,j}=d_x(D_x\phi)_{ij}+d_y(D_y\phi)_{ij}=\left(\phi_{i-1,j}+\phi_{i,j-1}-4\phi_{i,j}+\phi_{i,j+1}+\phi_{i+1,j}\right)/h^2,\\
&(\phi,\psi)_d=\sum_{i=1}^{N_x}\sum_{j=1}^{N_y}\phi_{i,j}\psi_{i,j},\quad A_d(\phi)=h^2\sum_{i=1}^{N_x}\sum_{j=1}^{N_y}\phi_{ij},\quad \|\phi\|_2^2=h^2(\phi,\phi)_d,
\end{aligned}$$

$$
\begin{aligned}
&(u, v)_{\mathrm{ew}} = \frac{1}{2}\sum_{i=1}^{m}\sum_{j=1}^{n}\left(u_{i+1/2,j}v_{i+1/2,j} + u_{i-1/2,j}v_{i-1/2,j}\right),\\
&(u, v)_{\mathrm{ns}} = \frac{1}{2}\sum_{i=1}^{m}\sum_{j=1}^{n}\left(u_{i,j+1/2}v_{i,j+1/2} + u_{i,j-1/2}v_{i,j-1/2}\right),\\
&\|\nabla_d\phi\|_2^2 = h^2\left(D_x\phi, D_x\phi\right)_{\mathrm{ew}} + h^2\left(D_y\phi, D_y\phi\right)_{\mathrm{ns}},\\
&\|\mathbf{u}\|_2^2 = h^2\left(u, u\right)_{\mathrm{ew}} + h^2\left(v, v\right)_{\mathrm{ns}},\\
&\|\nabla_d\mathbf{u}\|_2^2 = h^2\left(D_x u, D_x u\right)_{\mathrm{ew}} + h^2\left(D_y u, D_y u\right)_{\mathrm{ew}} + h^2\left(D_x v, D_x v\right)_{\mathrm{ns}} + h^2\left(D_y v, D_y v\right)_{\mathrm{ns}}.
\end{aligned}
\tag{19}
$$

Refer to [59,60], we can fine that the above weighted inner products satisfy the discrete Green's first identity and the Green's second identity.

3.1. Second-order accuracy scheme for the constrained formulation

In this section, we present a second-order numerical scheme for the thermal-fluid-based topology optimization problem with the constrained function Eqs. (7) and (8).

$$
\begin{aligned}
\frac{\phi^{n+1}-\phi^n}{\Delta t} = &-\frac{\gamma}{\epsilon}\left(F'\left(\tilde{\phi}^{n+\frac{1}{2}}\right) + \xi\phi^{n+\frac{1}{2}} - \xi\tilde{\phi}^{n+\frac{1}{2}}\right) + \gamma\epsilon\left(d_x\left(D_x\phi^{n+\frac{1}{2}}\right) + d_y\left(D_y\phi^{n+\frac{1}{2}}\right)\right),\\
&+\frac{\tilde{\alpha}_\epsilon}{2}\frac{|\mathbf{u}^n|^2 + |\mathbf{u}^{n+1}|^2}{2} - \beta\left(\frac{V\left(\phi^n\right) + V\left(\phi^{n+1}\right)}{2} - V_0\right),
\end{aligned}
\tag{20a}
$$

$$
D_x p^{n+\frac{1}{2}} - \left(d_x\left(\mu^{n+\frac{1}{2}}D_x u^{n+\frac{1}{2}}\right) + d_y\left(\mu^{n+\frac{1}{2}}D_y u^{n+\frac{1}{2}}\right)\right) + \frac{\alpha_\epsilon\left(\phi^n\right) + \alpha_\epsilon\left(\phi^{n+1}\right)}{2}u^{n+\frac{1}{2}} = \mathbf{f}^{x,n+\frac{1}{2}},
\tag{20b}
$$

$$
D_y p^{n+\frac{1}{2}} - \left(d_x\left(\mu^{n+\frac{1}{2}}D_x v^{n+\frac{1}{2}}\right) + d_y\left(\mu^{n+\frac{1}{2}}D_y v^{n+\frac{1}{2}}\right)\right) + \frac{\alpha_\epsilon\left(\phi^n\right) + \alpha_\epsilon\left(\phi^{n+1}\right)}{2}v^{n+\frac{1}{2}} = \mathbf{f}^{y,n+\frac{1}{2}},
\tag{20c}
$$

$$
d_x u^{n+1} + d_y v^{n+1} = 0,
\tag{20d}
$$

$$
\begin{aligned}
\frac{T^{n+1}-T^n}{\Delta t} - \frac{1}{\rho^{n+\frac{1}{2}}C_p^{n+\frac{1}{2}}}&\left(d_x K^{n+\frac{1}{2}}D_x T^{n+\frac{1}{2}} + d_y K^{n+\frac{1}{2}}D_y T^{n+\frac{1}{2}}\right)\\
&+ u^{n+\frac{1}{2}}D_x T^{n+\frac{1}{2}} + v^{n+\frac{1}{2}}D_y T^{n+\frac{1}{2}} = 0,
\end{aligned}
\tag{20e}
$$

where $\phi^{n+\frac{1}{2}} = (\phi^{n+1}+\phi^n)/2$, $\tilde{\phi}^{n+\frac{1}{2}} = (3\phi^n - \phi^{n-1})/2$, $\mu^{n+\frac{1}{2}} = (\mu^n + \mu^{n+1})/2$, $\mathbf{u}^{n+\frac{1}{2}} = (\mathbf{u}^{n+1}+\mathbf{u}^n)/2$, $\mathbf{f}^{x,n+\frac{1}{2}} = (\mathbf{f}^{x,n+1}+\mathbf{f}^{x,n})/2$, $\mathbf{f}^{y,n+\frac{1}{2}} = (\mathbf{f}^{y,n+1}+\mathbf{f}^{y,n})/2$, $K^{n+\frac{1}{2}} = (K^n + K^{n+1})/2$, $\rho^{n+\frac{1}{2}} = (\rho^n + \rho^{n+1})/2$, $C_p^{n+\frac{1}{2}} = (C_p^n + C_p^{n+1})/2$ and $T^{n+\frac{1}{2}} = (T^n + T^{n+1})/2$. We apply the following weighted inner products to deal with the boundary conditions as:

$$
\begin{aligned}
&(f, g)_{\mathrm{ew}} = -(1/h)\sum_{j=1}^{Ny} g_{1/2,j}f_{1/2,j} + (1/h)\sum_{j=1}^{ny} g_{nx+1/2,j}f_{nx+1/2,j}, \quad \text{if } f, g \in \mathcal{E}^{\mathrm{ew}}_{m\times n}\\
&(f, g)_{\mathrm{ns}} = -(1/h)\sum_{i=1}^{nx} g_{i,1/2}f_{i,1/2} + (1/h)\sum_{i=1}^{nx} g_{i,ny+1/2}f_{i,ny+1/2}, \quad \text{if } f, g \in \mathcal{E}^{\mathrm{ns}}_{m\times n}.
\end{aligned}
\tag{21}
$$

Then, we give the computational solutions of the proposed optimization system. Because the phase motion is coupled with the velocity field evolution, it is important to solve the Darcy equation and HT equation in a temporally matched manner. Here, ξ is a stabilizing parameter and satisfies $\xi \geq \max(F''(\phi)) = F''(\mathcal{M})$, where $\mathcal{M}$ is the maximum of ϕ.

Remark 1. We should point out that we restrict our attention to the order parameter ϕ which is bounded. The original Allen–Cahn(AC) equation satisfies the maximum principle refer to the existing discussions [61,62] on the maximum principle of ϕ. Our proposed hydrodynamic system is based on a modified AC equation, which may conserve the maximum principle. In addition, the double-well potential $F(\phi)$ restricted the growth of ϕ to be quadratic and return ϕ to the normal range. Although we cannot analytically prove ϕ is bounded in Eq. (20a) since $\mathbf{u}$ is coupled to ϕ and $F(\phi)$ exhibits quartic growth at infinity, our numerical experiments confirm that ϕ is bounded if the initial condition is set as $\phi^0 \in [0, 1]$. Thus, we assume that there exists $\mathcal{M}$, which is non-significantly larger than 1 and satisfies $|\phi| < \mathcal{M}$.

For the given initial ϕ^n, $\mathbf{u}^n$ and T^n, we compute ϕ^{n+1}, $\mathbf{u}^{n+1}$ and T^{n+1} by integrating the following steps:

Step 1. Update the phase ϕ^{n+1} with Eq. (20a) as

$$\begin{aligned}\frac{\phi^{n+1,q+1}-\phi^n}{\Delta t}=&-\frac{\gamma}{\epsilon}\left(F'\left(\tilde{\phi}^{n+\frac{1}{2}}\right)+\frac{\xi}{2}\left(\phi^{n+1,q+1}+\phi^n\right)-\xi\tilde{\phi}^{n+\frac{1}{2}}\right)\\&+\gamma\epsilon\left(d_x\left(D_x\left(\phi^{n+1,q+1}+\phi^n\right)\right)+d_y\left(D_y\left(\phi^{n+1,q+1}+\phi^n\right)\right)\right)\\&+\frac{\tilde{\alpha}_\epsilon}{2}\frac{|\mathbf{u}^n|^2+|\mathbf{u}^{n+1}|^2}{2}-\beta\left(\frac{V_d\left(\phi^n\right)+V_d\left(\phi^{n+1,q}\right)}{2}-V_0\right),\end{aligned}\tag{22}$$

where q is the index of Picard iteration and we apply the procedure until $\left\|\phi^{n+1,q+1}-\phi^{n+1,q}\right\|_d^2\le tol$.

Step 2. Take the divergence operator to both sides of Eq. (20b) and update the pressure p^{n+1} as:

$$\begin{aligned}&d_x\left(D_xp^{n+\frac{1}{2}}\right)+d_y\left(D_yp^{n+\frac{1}{2}}\right)=d_x\mathbf{f}^{x,n+\frac{1}{2}}+d_y\mathbf{f}^{y,n+\frac{1}{2}}\\&\quad-\frac{1}{4}\left(d_x\left(\left(u^n+u^{n+1,m}\right)A_x\left(\alpha_\epsilon\left(\phi^n\right)+\alpha_\epsilon\left(\phi^{n+1}\right)\right)\right)+d_y\left(\left(v^n+v^{n+1,m}\right)A_y\left(\alpha_\epsilon\left(\phi^n\right)+\alpha_\epsilon\left(\phi^{n+1}\right)\right)\right)\right).\end{aligned}$$

Update the velocity field $\mathbf{u}^{n+1}$ with Eq. (20b) as:

$$\begin{aligned}&\mu^{n+\frac{1}{2}}\left(d_x(D_xu^{n+\frac{1}{2}})+d_y(D_yv^{n+\frac{1}{2}})\right)-\frac{\alpha_\epsilon\left(\phi^n\right)+\alpha_\epsilon\left(\phi^{n+1}\right)}{2}u^{n+\frac{1}{2}}=D_xp^{n+\frac{1}{2}}-\mathbf{f}^{x,n+\frac{1}{2}},\\&\mu^{n+\frac{1}{2}}\left(d_x(D_xu^{n+\frac{1}{2}})+d_y(D_yv^{n+\frac{1}{2}})\right)-\frac{\alpha_\epsilon\left(\phi^n\right)+\alpha_\epsilon\left(\phi^{n+1}\right)}{2}v^{n+\frac{1}{2}}=D_yp^{n+\frac{1}{2}}-\mathbf{f}^{y,n+\frac{1}{2}}.\end{aligned}\tag{23}$$

To obtain the solution of the pressure and velocity field, we employ a Picard iteration as follows:

$$\begin{aligned}&d_x\left(D_xp^{n+1,m+1}\right)+d_y\left(D_yp^{n+1,m+1}\right)+d_x\left(D_xp^n\right)+d_y\left(D_yp^n\right)=2d_x\mathbf{f}^{x,n+\frac{1}{2}}+2d_y\mathbf{f}^{y,n+\frac{1}{2}}\\&-\frac{1}{2}\left(d_x\left(\left(u^n+u^{n+1,m}\right)A_x\left(\alpha_\epsilon\left(\phi^n\right)+\alpha_\epsilon\left(\phi^{n+1}\right)\right)\right)+d_y\left(\left(v^n+v^{n+1,m}\right)A_y\left(\alpha_\epsilon\left(\phi^n\right)+\alpha_\epsilon\left(\phi^{n+1}\right)\right)\right)\right),\\&\frac{\mu^{n+\frac{1}{2}}}{2}\left(d_x\left(D_xu^{n+1,m+1}\right)+d_y\left(D_yu^{n+1,m+1}\right)\right)-\frac{\alpha_\epsilon(\phi^n)+\alpha_\epsilon(\phi^{n+1})}{2}\frac{u^{n+1,m+1}}{2}\\&\quad=\frac{D_xp^{n+1,m+1}+D_xp^n}{2}+\frac{\alpha_\epsilon(\phi^n)+\alpha_\epsilon(\phi^{n+1})}{2}\frac{u^n}{2}-\mathbf{f}^{x,n+\frac{1}{2}}-\frac{\mu^{n+\frac{1}{2}}}{2}\left(d_x\left(D_xu^n\right)+d_y\left(D_yu^n\right)\right),\\&\frac{\mu^{n+\frac{1}{2}}}{2}\left(d_x\left(D_xv^{n+1,m+1}\right)+d_y\left(D_yv^{n+1,m+1}\right)\right)-\frac{\alpha_\epsilon(\phi^n)+\alpha_\epsilon(\phi^{n+1})}{2}\frac{v^{n+1,m+1}}{2}\\&\quad=\frac{D_yp^{n+1,m+1}+D_yp^n}{2}+\frac{\alpha_\epsilon(\phi^n)+\alpha_\epsilon(\phi^{n+1})}{2}\frac{v^n}{2}-\mathbf{f}^{y,n+\frac{1}{2}}-\frac{\mu^{n+\frac{1}{2}}}{2}\left(d_x\left(D_xv^n\right)+d_y\left(D_yv^n\right)\right),\end{aligned}$$

where m is the index of Picard iteration and we compute until

$$\left\|p^{n+1,m+1}-p^{n+1,m}\right\|_2^2+\left\|\mathbf{u}^{n+1,m+1}-\mathbf{u}^{n+1,m}\right\|_2^2\le tol.\tag{24}$$

Step 3. Update the temperature field with Eq. (20e) as:

$$\frac{T^{n+1}-T^n}{\Delta t}+u^{n+\frac{1}{2}}D_xT^{n+\frac{1}{2}}+v^{n+\frac{1}{2}}D_yT^{n+\frac{1}{2}}=\frac{1}{\rho^{n+\frac{1}{2}}C_p^{n+\frac{1}{2}}}\left(d_xK^{n+\frac{1}{2}}D_xT^{n+\frac{1}{2}}+d_yK^{n+\frac{1}{2}}D_yT^{n+\frac{1}{2}}\right).\tag{25}$$

Some notations should be pointed here: (i) We use two level values, i.e., ϕ^{-1}, ϕ^0, $\mathbf{u}^{-1}$, $\mathbf{u}^0$, T^{-1} and T^0, to initialize the computation. Let us set $\phi^{-1}:=\phi^0$, $\mathbf{u}^{-1}:=\mathbf{u}^0$ and $T^{-1}:=T^0$, which will not reduce the accuracy of the numerical scheme. (ii) $V(\phi^{n+1})$ in nonlinear with respect to ϕ^{n+1} in Eq. (20a) by taking the inner product of Eq. (20a) with $\mathbf{1}$ and using the definition of $V(\phi)$. Thus the Picard iterations is needed to makes the original nonlinear problem become a linear solvable problem. (iii) There are also other efficient algorithms, such as Newton's method and conjugate gradient method, to solve the proposed model. In order to match the theoretical proof of energy dissipation, we adopt the above algorithm. (iv) The central difference scheme is used for spatial discretization and the Crank–Nicolson type scheme is used for temporal discretization, which are both second-order accurate. We will not prove but imply a numerical test to verify that our algorithm conforms to second-order accuracy.

3.2. Unconditional stability for the numerical scheme

In this subsection, we demonstrate the unconditional stability of the proposed scheme Eq. (20). Let us define the modified energy as

$$\tilde{J}_d\left(\phi^{n+1},\phi^n,\mathbf{u}^{n+1},T^{n+1}\right)=J_d\left(\phi^{n+1},\mathbf{u}^{n+1},T^{n+1}\right)+\frac{\xi-F''\left(\sigma^{n,n+1}\right)}{4\epsilon}\gamma\left\|\phi^{n+1}-\phi^n\right\|_2^2, \tag{26}$$

where the total energy is defined as

$$\begin{aligned}&J_d\left(\phi^n,\mathbf{u}^n,T^n\right)\\&=\frac{\mu^{n+\frac{1}{2}}}{2}\|\nabla_d\mathbf{u}^n\|_2^2-\left(\mathbf{u}^n,\mathbf{f}^n\right)_d+\gamma\left(\frac{\epsilon}{2}\|\nabla_d\phi^n\|_2^2+\frac{1}{\epsilon}\left(F\left(\phi^n\right),\mathbf{1}\right)_d\right)\\&+\frac{\alpha(\phi^n)}{2}\|\mathbf{u}^n\|_2^2+\frac{\|T^n\|_2^2}{2}+\frac{\beta}{2}\left(V\left(\phi^n\right)-V_0,V\left(\phi^n\right)-V_0\right)_d\end{aligned} \tag{27}$$

and $\sigma^{n,n+1}$ satisfies the following functional:

$$\begin{aligned}&\left(F'(\tilde{\phi}^{n+\frac{1}{2}}),\phi^{n+1}-\phi^n\right)_d=\left(F(\phi^{n+1})-F(\phi^n),\mathbf{1}\right)_d\\&-\frac{F''\left(\sigma^{n,n+1}\right)}{4}\left(\left\|\phi^{n+1}-\phi^n\right\|_2^2-\left\|\phi^n-\phi^{n-1}\right\|_2^2+\left\|\phi^{n+1}-2\phi^n+\phi^{n-1}\right\|_2^2\right).\end{aligned} \tag{28}$$

Theorem 3. *If $\xi\geq F''(\mathcal{M})$, the solutions of Eq. (20) make the modified energy decay with respect to time:*

$$\begin{aligned}&\tilde{J}_d(\phi^{n+1},\phi^n,\mathbf{u}^{n+1},T^{n+1})-\tilde{J}_d(\phi^n,\phi^{n-1},\mathbf{u}^n,T^n)\\&=-\frac{1}{\Delta t}\left\|\phi^{n+1}-\phi^n\right\|_2^2-\Delta tK^{n+\frac{1}{2}}\left\|\nabla_dT^{n+\frac{1}{2}}\right\|_2^2-\frac{\xi-F''\left(\sigma^{n+1,n}\right)}{4\epsilon}\gamma\left\|\phi^{n+1}-2\phi^n+\phi^{n-1}\right\|_2^2\leq 0.\end{aligned} \tag{29}$$

Proof. By multiplying Eq. (20b) with $u^{n+1}-u^n$ and Eq. (20c) with $v^{n+1}-v^n$, we can obtain the following function:

$$\begin{aligned}&\frac{\mu^{n+\frac{1}{2}}}{2}\left((D_xu^{n+1},D_xu^{n+1})_{\mathrm{ew}}+(D_yu^{n+1},D_yu^{n+1})_{\mathrm{ew}}-(D_xu^n,D_xu^n)_{\mathrm{ew}}-(D_yu^n,D_yu^n)_{\mathrm{ew}}\right)\\&+\frac{1}{2}\left(\alpha_\epsilon(\phi^{n+1})u^{n+1},u^{n+1}\right)_{\mathrm{ew}}-\frac{1}{2}\left(\alpha_\epsilon(\phi^n)u^n,u^n\right)_{\mathrm{ew}}-\left(\mathbf{f}^{x,n+1},u^{n+1}\right)_{\mathrm{ew}}+\left(\mathbf{f}^{x,n},u^n\right)_{\mathrm{ew}}\\&=\frac{1}{4}\left(\alpha_\epsilon(\phi^{n+1})-\alpha_\epsilon(\phi^n),(u^{n+1},u^{n+1})_{\mathrm{ew}}+(u^n,u^n)_{\mathrm{ew}}\right)_{\mathrm{ew}},\end{aligned} \tag{30a}$$

and

$$\begin{aligned}&\frac{\mu^{n+\frac{1}{2}}}{2}\left((D_xv^{n+1},D_xv^{n+1})_{\mathrm{ns}}+(D_yv^{n+1},D_yv^{n+1})_{\mathrm{ns}}-(D_xv^n,D_xv^n)_{\mathrm{ns}}-(D_yv^n,D_yv^n)_{\mathrm{ns}}\right)\\&+\frac{1}{2}\left(\alpha_\epsilon(\phi^{n+1})v^{n+1},v^{n+1}\right)_{\mathrm{ns}}-\frac{1}{2}\left(\alpha_\epsilon(\phi^n)v^n,v^n\right)_{\mathrm{ns}}-\left(\mathbf{f}^{y,n+1},v^{n+1}\right)_{\mathrm{ns}}+\left(\mathbf{f}^{y,n},v^n\right)_{\mathrm{ns}}\\&=\frac{1}{4}\left(\alpha_\epsilon(\phi^{n+1})-\alpha_\epsilon\left(\phi^n\right),(v^{n+1},v^{n+1})_{\mathrm{ns}}+(v^n,v^n)_{\mathrm{ns}}\right)_{\mathrm{ns}}.\end{aligned} \tag{30b}$$

By taking the inner product with Eq. (20a) and $-(\phi^{n+1}-\phi^n)$, we obtain the following equation:

$$\begin{aligned}&-\frac{1}{\Delta t}(\phi^{n+1}-\phi^n,\phi^{n+1}-\phi^n)_d\\&=\frac{\gamma}{\epsilon}\left(F'(\tilde{\phi}^{n+\frac{1}{2}}),\phi^{n+1}-\phi^n\right)_d+\frac{\xi\gamma}{\epsilon}\left(\phi^{n+\frac{1}{2}}-\tilde{\phi}^{n+\frac{1}{2}},\phi^{n+1}-\phi^n\right)_d\\&-\epsilon\gamma\left(d_x\left(D_x\phi^{n+\frac{1}{2}}\right),\phi^{n+1}-\phi^n\right)_{\mathrm{ew}}-\epsilon\gamma\left(+d_y(D_y\phi^{n+\frac{1}{2}}),\phi^{n+1}-\phi^n\right)_{\mathrm{ns}}\\&+\left(\frac{\alpha'_\epsilon\left(\phi^n\right)+\alpha'_\epsilon\left(\phi^{n+1}\right)}{4}\frac{|\mathbf{u}^n|^2+|\mathbf{u}^{n+1}|^2}{2},\phi^{n+1}-\phi^n\right)_d\\&+\frac{\beta}{2}\left(V_d(\phi^{n+1})+V_d(\phi^n)-2V_0,\phi^{n+1}-\phi^n\right)_d\\&=\frac{\gamma}{\epsilon}\left(F'(\tilde{\phi}^{n+\frac{1}{2}}),\phi^{n+1}-\phi^n\right)_d+\frac{\xi\gamma}{4\epsilon}\left((\phi^{n+1}-\phi^n,\phi^{n+1}-\phi^n)_d-\left(\phi^n-\phi^{n-1},\phi^n-\phi^{n-1}\right)_d\right.\end{aligned} \tag{31}$$

$$+(\phi^{n+1}-2\phi^{n}+\phi^{n-1},\phi^{n+1}-2\phi^{n}+\phi^{n-1})_d)+\frac{\gamma\epsilon}{2}(D_x\phi^{n+1},D_x\phi^{n+1})_{\mathrm{ew}}+\frac{\gamma\epsilon}{2}(D_y\phi^{n+1},D_y\phi^{n+1})_{\mathrm{ns}}$$
$$-\frac{\gamma\epsilon}{2}\left(D_x\phi^{n},D_x\phi^{n}\right)_{\mathrm{ew}}-\frac{\gamma\epsilon}{2}\left(D_y\phi^{n},D_y\phi^{n}\right)_{\mathrm{ns}}-\left(\alpha_\epsilon\left(\phi^{n+1}\right)-\alpha_\epsilon\left(\phi^{n}\right),\frac{|\mathbf{u}^{n}|^2+|\mathbf{u}^{n+1}|^2}{4}\right)_d$$
$$+\frac{\beta}{2}\left(V_d\left(\phi^{n+1}\right)-V_0,V_d\left(\phi^{n+1}\right)-V_0\right)_d-\frac{\beta}{2}\left(V_d(\phi^{n})-V_0,V_d\left(\phi^{n}\right)-V_0\right)_d.$$

By taking the inner product with Eq. (20e) and $T^{n+\frac{1}{2}}/\left(\rho^{n+\frac{1}{2}}C_p^{n+\frac{1}{2}}\right)$, we can obtain the following:

$$\begin{aligned}
&\frac{1}{2\Delta t}\left(T^{n+1}-T^{n},T^{n+1}+T^{n}\right)_d\\
&=-\left(u^{n+\frac{1}{2}}D_xT^{n+\frac{1}{2}},T^{n+\frac{1}{2}}\right)_{\mathrm{ew}}-\left(v^{n+\frac{1}{2}}D_yT^{n+\frac{1}{2}},T^{n+\frac{1}{2}}\right)_{\mathrm{ns}}\\
&\quad+\frac{1}{\rho^{n+\frac{1}{2}}C_p^{n+\frac{1}{2}}}\left((d_x(K^{n+\frac{1}{2}}D_xT^{n+\frac{1}{2}}),T^{n+\frac{1}{2}})_{\mathrm{ew}}+(d_y(K^{n+\frac{1}{2}}D_yT^{n+\frac{1}{2}}),T^{n+\frac{1}{2}})_{\mathrm{ns}}\right)\\
&=-\left(u^{n+\frac{1}{2}}D_xT^{n+\frac{1}{2}},T^{n+\frac{1}{2}}\right)_{\mathrm{ew}}-\left(v^{n+\frac{1}{2}}D_yT^{n+\frac{1}{2}},T^{n+\frac{1}{2}}\right)_{\mathrm{ns}}\\
&\quad-\frac{1}{\rho^{n+\frac{1}{2}}C_p^{n+\frac{1}{2}}}\left((K^{n+\frac{1}{2}}D_xT^{n+\frac{1}{2}},D_xT^{n+\frac{1}{2}})_{\mathrm{ew}}+(K^{n+\frac{1}{2}}D_yT^{n+\frac{1}{2}},D_yT^{n+\frac{1}{2}})_{\mathrm{ns}}\right),
\end{aligned}\tag{32}$$

Since that $\left(u^{n+\frac{1}{2}}D_xT^{n+\frac{1}{2}}+v^{n+\frac{1}{2}}D_yT^{n+\frac{1}{2}},T^{n+\frac{1}{2}}\right)_d=0$ has been proved in [63], thus

$$\frac{1}{2}\left(T^{n+1}-T^{n},T^{n+1}+T^{n}\right)_d=-\frac{\Delta tK^{n+\frac{1}{2}}}{\rho^{n+\frac{1}{2}}C_p^{n+\frac{1}{2}}}\left((D_xT^{n+\frac{1}{2}},D_xT^{n+\frac{1}{2}})_{\mathrm{ew}}+(D_yT^{n+\frac{1}{2}},D_yT^{n+\frac{1}{2}})_{\mathrm{ns}}\right).$$

Considering the term $F\left(\phi^{n+1}\right)-F\left(\phi^{n}\right)$ with the Taylor expansion as:

$$\begin{aligned}
&\left(F(\phi^{n+1})-F(\phi^{n}),\mathbf{1}\right)_d\\
&=\left(F(\phi^{n+1}),\mathbf{1}\right)_d-\left(F(\tilde{\phi}^{n+\frac{1}{2}}),\mathbf{1}\right)_d+\left(F(\tilde{\phi}^{n+\frac{1}{2}}),\mathbf{1}\right)_d-\left(F(\phi^{n}),\mathbf{1}\right)_d\\
&=\left(F'(\tilde{\phi}^{n+\frac{1}{2}}),\phi^{n+1}-\tilde{\phi}^{n+\frac{1}{2}}\right)_d+\left(\frac{F''\left(\zeta_1^{n+1}\right)}{2}\left(\phi^{n+1}-\tilde{\phi}^{n+\frac{1}{2}}\right),\phi^{n+1}-\tilde{\phi}^{n+\frac{1}{2}}\right)_d\\
&\quad-\left(F'(\tilde{\phi}^{n+\frac{1}{2}}),\phi^{n}-\tilde{\phi}^{n+\frac{1}{2}}\right)_d-\left(\frac{F''\left(\zeta_2^{n}\right)}{2}(\phi^{n}-\tilde{\phi}^{n+\frac{1}{2}}),\phi^{n}-\tilde{\phi}^{n+\frac{1}{2}}\right)_d\\
&=\left(F'(\tilde{\phi}^{n+\frac{1}{2}}),\phi^{n+1}-\phi^{n}\right)_d+\frac{F''\left(\sigma^{n+1,n}\right)}{4}\Big(\left(\phi^{n}-\phi^{n-1},\phi^{n}-\phi^{n-1}\right)_d-\left(\phi^{n+1}-\phi^{n},\phi^{n+1}-\phi^{n}\right)_d\\
&\quad-\left(\phi^{n+1}-2\phi^{n}+\phi^{n-1},\phi^{n+1}-2\phi^{n}+\phi^{n-1}\right)_d\Big),
\end{aligned}\tag{33}$$

where the three constants ζ_1^{n+1}, ζ_2^{n}, and $\sigma^{n+1,n}$ can be obtained based on the Cauchy's mean value theorem [64]. Thus, we obtain the energy dissipation by multiplying the above equation with $h^2/2$ and summing them as:

$$\begin{aligned}
&\tilde{J}_d\left(\phi^{n+1},\phi^{n},\mathbf{u}^{n+1},T^{n+1}\right)-\tilde{J}_d\left(\phi^{n},\phi^{n-1},\mathbf{u}^{n},T^{n}\right)\\
&=\frac{\mu^{n+\frac{1}{2}}}{2}\left(\left\|\nabla_d\mathbf{u}^{n+1}\right\|_2^2-\left\|\nabla_d\mathbf{u}^{n}\right\|_2^2\right)-\left(\mathbf{u}^{n+1}-\mathbf{u}^{n},\mathbf{f}\right)_d+\frac{\gamma\epsilon}{2}\left(\left\|\nabla\phi^{n+1}\right\|_2^2-\left\|\nabla\phi^{n}\right\|_2^2\right)\\
&\quad+\frac{\gamma}{\epsilon}\left(F\left(\phi^{n+1}\right)-F\left(\phi^{n}\right),\mathbf{1}\right)_d+\frac{\alpha_\epsilon\left(\phi^{n+1}\right)}{2}\left\|\mathbf{u}^{n+1}\right\|_2^2-\frac{\alpha_\epsilon\left(\phi^{n}\right)}{2}\left\|\mathbf{u}^{n}\right\|_2^2\\
&\quad+\frac{1}{2}\left(\left\|T^{n+1}\right\|_2^2-\left\|T^{n}\right\|_2^2\right)+\frac{\beta}{2}\left(\left(V\left(\phi^{n+1}\right)-V_0\right)^2-\left(V\left(\phi^{n}\right)-V_0\right)^2,\mathbf{1}\right)_d\\
&\quad+\frac{\zeta-F''\left(\sigma^{n+1,n}\right)}{4\epsilon}\gamma\left(\left\|\phi^{n+1}-\phi^{n}\right\|_2^2-\left\|\phi^{n}-\phi^{n-1}\right\|_2^2\right)\\
&=\frac{\mu^{n+\frac{1}{2}}h^2}{2}\left((D_xu^{n+1},D_xu^{n+1})_{\mathrm{ew}}+(D_yu^{n+1},D_yu^{n+1})_{\mathrm{ew}}+(D_xv^{n+1},D_xv^{n+1})_{\mathrm{ns}}+(D_yv^{n+1},D_yv^{n+1})_{\mathrm{ns}}\right.\\
&\quad\left.-\left(D_xu^{n},D_xu^{n}\right)_{\mathrm{ew}}-\left(D_yu^{n},D_yu^{n}\right)_{\mathrm{ew}}-\left(D_xv^{n},D_xv^{n}\right)_{\mathrm{ns}}-\left(D_yv^{n},D_yv^{n}\right)_{\mathrm{ns}}\right)
\end{aligned}$$

$$
\begin{aligned}
&-\left(u^{n+1}-u^{n}, \mathbf{f}^{x,n+\frac{1}{2}}\right)_{\mathrm{ew}}-\left(v^{n+1}-v^{n}, \mathbf{f}^{y,n+\frac{1}{2}}\right)_{\mathrm{ns}}\\
&+\frac{\gamma\epsilon h^{2}}{2}\left(\left(D_{x}\phi^{n+1}, D_{x}\phi^{n+1}\right)_{\mathrm{ew}}+\left(D_{y}\phi^{n+1}, D_{y}\phi^{n+1}\right)_{\mathrm{ns}}\right.\\
&\left.-\left(D_{x}\phi^{n}, D_{x}\phi^{n}\right)_{\mathrm{ew}}-\left(D_{y}\phi^{n}, D_{y}\phi^{n}\right)_{\mathrm{ns}}\right)+\frac{\gamma}{\epsilon}\left(F(\phi^{n+1})-F\left(\phi^{n}\right), \mathbf{1}\right)_{d}\\
&+\frac{\alpha_{\epsilon}\left(\phi^{n+1}\right)h^{2}}{2}\left(\left(u^{n+1}, u^{n+1}\right)_{\mathrm{ew}}+\left(v^{n+1}, v^{n+1}\right)_{\mathrm{ns}}\right)-\frac{\alpha_{\epsilon}\left(\phi^{n}\right)h^{2}}{2}\left(\left(u^{n}, u^{n}\right)_{\mathrm{ew}}+\left(v^{n}, v^{n}\right)_{\mathrm{ns}}\right)\\
&+\frac{h^{2}}{2}\left(\left(T^{n+1}, T^{n+1}\right)_{d}-\left(T^{n}, T^{n}\right)_{d}\right)+\frac{\beta}{2}\left(\left(V\left(\phi^{n+1}\right)-V_{0}\right)^{2}-\left(V\left(\phi^{n}\right)-V_{0}\right)^{2}, \mathbf{1}\right)_{d}\\
&+\frac{\zeta-F''\left(\sigma^{n+1,n}\right)}{4\epsilon}\gamma\left(h^{2}(\phi^{n+1}-\phi^{n}, \phi^{n+1}-\phi^{n})_{d}-h^{2}(\phi^{n}-\phi^{n-1}, \phi^{n}-\phi^{n-1})_{d}\right)\\
=&\frac{\alpha_{\epsilon}\left(\phi^{n+1}\right)-\alpha_{\epsilon}\left(\phi^{n}\right)}{4}h^{2}\left(\left(u^{n+1}, u^{n+1}\right)_{\mathrm{ew}}+\left(v^{n+1}, v^{n+1}\right)_{\mathrm{ns}}\right)\\
&+\frac{\alpha_{\epsilon}\left(\phi^{n+1}\right)-\alpha_{\epsilon}\left(\phi^{n}\right)}{4}h^{2}\left(\left(u^{n}, u^{n}\right)_{\mathrm{ew}}+\left(v^{n}, v^{n}\right)_{\mathrm{ns}}\right)\\
&+\frac{\gamma\epsilon h^{2}}{2}\left(\left(D_{x}\phi^{n+1}, D_{x}\phi^{n+1}\right)_{\mathrm{ew}}+\left(D_{y}\phi^{n+1}, D_{y}\phi^{n+1}\right)_{\mathrm{ns}}-\left(D_{x}\phi^{n}, D_{x}\phi^{n}\right)_{\mathrm{ew}}-\left(D_{y}\phi^{n}, D_{y}\phi^{n}\right)_{\mathrm{ns}}\right)\\
&+\frac{\gamma}{\epsilon}\left(F(\phi^{n+1})-F(\phi^{n}), \mathbf{1}\right)_{d}+\frac{\beta}{2}\left(\left(V\left(\phi^{n+1}\right)-V_{0}\right)^{2}-\left(V\left(\phi^{n}\right)-V_{0}\right)^{2}, \mathbf{1}\right)_{d}\\
&+\frac{h^{2}}{2}\left(T^{n+1}-T^{n}, T^{n+1}+T^{n}\right)_{d}\\
&+\frac{\zeta-F''\left(\sigma^{n+1,n}\right)}{4\epsilon}\gamma\left(h^{2}\left(\phi^{n+1}-\phi^{n}, \phi^{n+1}-\phi^{n}\right)_{d}-h^{2}\left(\phi^{n}-\phi^{n-1}, \phi^{n}-\phi^{n-1}\right)_{d}\right)\\
=&-\frac{h^{2}}{\Delta t}\left(\phi^{n+1}-\phi^{n}, \phi^{n+1}-\phi^{n}\right)_{d}-\frac{\gamma}{\epsilon}\left(F'(\tilde{\phi}^{n+\frac{1}{2}}), \phi^{n+1}-\phi^{n}\right)_{d}\\
&-\frac{\xi\gamma h^{2}}{4\epsilon}\left(\left(\phi^{n+1}-\phi^{n}, \phi^{n+1}-\phi^{n}\right)_{d}-\left(\phi^{n}-\phi^{n-1}, \phi^{n}-\phi^{n-1}\right)_{d}\right.\\
&\left.+(\phi^{n+1}-2\phi^{n}+\phi^{n-1}, \phi^{n+1}-2\phi^{n}+\phi^{n-1})_{d}\right)+\frac{\gamma}{\epsilon}\left(F(\phi^{n+1})-F\left(\phi^{n}\right), \mathbf{1}\right)_{d}\\
&-\frac{\Delta tK^{n+\frac{1}{2}}h^{2}}{\rho^{n+\frac{1}{2}}C_{p}^{n+\frac{1}{2}}}\left(\left(D_{x}T^{n+\frac{1}{2}}, D_{x}T^{n+\frac{1}{2}}\right)_{\mathrm{ew}}+\left(D_{y}T^{n+\frac{1}{2}}, D_{y}T^{n+\frac{1}{2}}\right)_{\mathrm{ns}}\right)\\
&+\frac{\zeta-F''\left(\sigma^{n+1,n}\right)}{4\epsilon}\gamma\left(h^{2}(\phi^{n+1}-\phi^{n}, \phi^{n+1}-\phi^{n})_{d}-h^{2}\left(\phi^{n}-\phi^{n-1}, \phi^{n}-\phi^{n-1}\right)_{d}\right)\\
=&-\frac{1}{\Delta t}\left\|\phi^{n+1}-\phi^{n}\right\|_{d}^{2}-\frac{\gamma}{\epsilon}\left(F'(\tilde{\phi}^{n+\frac{1}{2}}), \phi^{n+1}-\phi^{n}\right)_{d}+\frac{\gamma}{\epsilon}\left(F\left(\phi^{n+1}\right)-F\left(\phi^{n}\right), \mathbf{1}\right)_{d}\\
&-\frac{\Delta tK^{n+\frac{1}{2}}}{\rho^{n+\frac{1}{2}}C_{p}^{n+\frac{1}{2}}}\left\|\nabla_{d}T^{n+\frac{1}{2}}\right\|_{2}^{2}-\frac{\xi-F''\left(\sigma^{n+1,n}\right)}{4\epsilon}\gamma\left\|\phi^{n+1}-2\phi^{n}+\phi^{n-1}\right\|_{2}^{2}\\
=&-\frac{1}{\Delta t}\left\|\phi^{n+1}-\phi^{n}\right\|_{2}^{2}-\frac{\Delta tK^{n+\frac{1}{2}}}{\rho^{n+\frac{1}{2}}C_{p}^{n+\frac{1}{2}}}\left\|\nabla_{d}T^{n+\frac{1}{2}}\right\|_{2}^{2}-\frac{\xi-F''\left(\sigma^{n+1,n}\right)}{4\epsilon}\gamma\left\|\phi^{n+1}-2\phi^{n}+\phi^{n-1}\right\|_{2}^{2}\leq 0,
\end{aligned}
$$

which corresponds to Eq. (29). □

Remark 2. We should remark that the present framework with the modified energy convergences to the original optimization problem. Although we cannot prove that the original energy is unconditional decreasing, we can see that the original energy is bounded by the modified energy, i.e., $J_d\left(\phi^n, \mathbf{u}^n, T^n\right) \leq \tilde{J}_d\left(\phi^n, \mathbf{u}^n, T^n\right)+\frac{\xi-F''\left(\sigma^{n,n+1}\right)}{4\epsilon}\gamma\left\|\phi^{n+1}-\phi^n\right\|_d^2$ if $\xi \geq F''(\mathcal{M})$. Let us denote $\{\phi^n, \mathbf{u}^n, T^n\}$ as the solution of Eqs. (20) in a iteration, which starts with initial values $\left\{\phi^0, \mathbf{u}^0, T^0\right\}$ and $\left\{\phi^{-1}, \mathbf{u}^{-1}, T^{-1}\right\}$. Here $\phi^{-1}=\phi^0$, $\mathbf{u}^{-1}=\mathbf{u}^0$ and $T^{-1}=T^0$. With the assumption $\xi \geq F''(\mathcal{M})$, the following inequality can be obtained:

$$
J_d\left(\phi^{n+1}, \mathbf{u}^{n+1}, T^{n+1}\right)-\tilde{J}_d\left(\phi^{n+1}, \phi^n, \mathbf{u}^{n+1}, T^{n+1}\right)=-\frac{\xi-F''\left(\sigma^{n,n+1}\right)}{4\epsilon}\gamma\left\|\phi^{n+1}-\phi^n\right\|_2^2 \leq 0,
$$

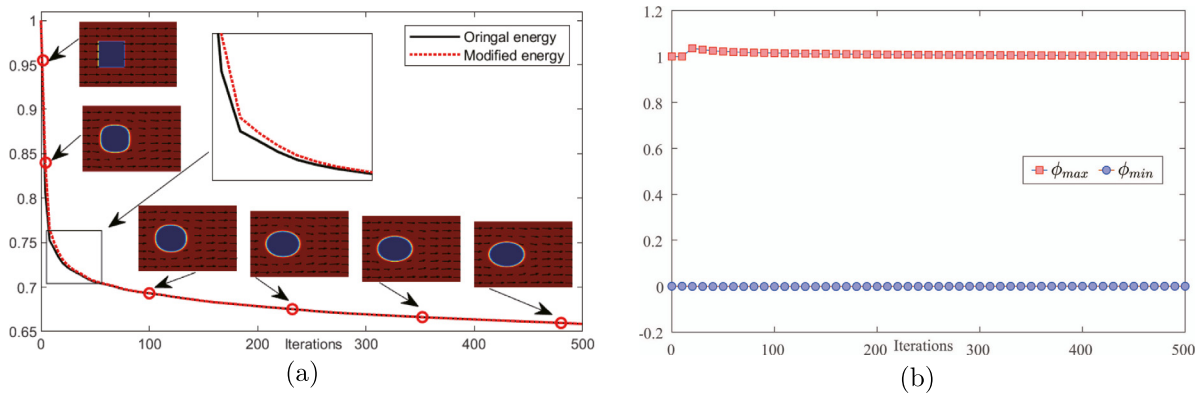

Fig. 1. Temporal evolution of (a) the discrete modified and original energies using the proposed scheme and (b) the maximum and minimum value of ϕ.

which implies that

$$J_d\left(\phi^{n+1}, \mathbf{u}^{n+1}, T^{n+1}\right) \leq \tilde{J}_d\left(\phi^{n+1}, \phi^n, \mathbf{u}^{n+1}, T^{n+1}\right) \leq \cdots \leq \tilde{J}_d\left(\phi^0, \phi^{-1}, \mathbf{u}^0, T^0\right) = J_d\left(\phi^0, \mathbf{u}^0, T^0\right).$$

Thus, the original discrete energy is bounded by the modified energy, which is indeed non-increasing with respect to time. Despite it is difficult to prove that the original optimization problem (Eqs. (6)–(8)) satisfies a energy dissipation law, the results of the numerical tests presented in Section 4 indicate that the original energy $J(\phi, \mathbf{u})$ is non-increasing.

4. Numerical results

We present computational tests to demonstrate the efficiency of the proposed method. Unless otherwise specified, we will choose the computational domain as $\Omega = [0, 10] \times [0, 10]$ with a 512×512 mesh grid. The following parameters for the numerical simulations are chosen as: $\mu_1 : \mu_2 = C_1 : C_2 = K_1 : K_2 = 1 : 1$, $\epsilon = 4h/(4\sqrt{2}\text{atanh}(0.9))$, $\tilde{\alpha}_\epsilon = 10$, $\beta = 10$, $\gamma = 0.5$, $\xi = 0.5$ and $\Delta t = 0.5h$. The external force $\mathbf{f} = (10, 0)$ is imposed in the local circular region with center $[5, 5]$ and radius $r = 1$. We use the Dirichlet boundary condition for the phase-field ϕ, the velocity field $\mathbf{u}$ and the temperature field T. The Neumann boundary condition is used for the pressure field p.

4.1. Non-increasing discrete energy test

To demonstrate the energy decrease, we study the temporal evolution of the scaled discrete energy $J_d(\phi^n)/J_d(\phi^0)$. We apply the numerical test of the design of rugby in the computational domain $\Omega = [0, 15] \times [0, 10]$ with a 768×512 mesh grid. The initial conditions are chosen as follows:

$$\begin{cases} \phi(x, y, 0) = 0.5 - 0.5 \tanh\left(-\max\left(|x - 5| - 2,\ |y - 5| - 2\right)/\left(\sqrt{2}\epsilon\right)\right), \\ \mathbf{u}(x, y, 0) = (5\phi(x, y, 0), 0), \\ T(x, y, 0) = T_0\phi(x, y, 0). \end{cases} \tag{36}$$

Here we choose the non-default parameters as follows: $T_0 = 20$, $\gamma = 0.01$ and $V_0 = 16$. The inset figures are the morphology of the phase field at the indicated times. The velocity fields during the evolution process are presented on the sub-figures. The modified energy and the original energy have been normalized by the initial energy. The results of shown in Fig. 1(a) suggest that the fluid goes from left to right away from the obstacle and the solid shape becomes an ellipse. Furthermore, we can observe that the modified energy dissipates during the evolution. We also can find that the original discrete energy is bounded by the modified energy and non-increasing. Furthermore, we have shown in Fig. 1(b) that the value of ϕ is essentially bounded. The slight deviation of ϕ from the value range is caused by $\alpha'_\epsilon(\phi)|\mathbf{u}|^2/2$. However, since the double-well potential $F(\phi)$ restricted the growth of ϕ to be quadratic, ϕ is boundedness.

4.2. Convergence test

We implement two computational tests of the temporal and spatial truncation errors to demonstrate the convergence of our scheme. Because the governing equations have no closed-form analytical solution, we use the numerical solution obtained by very fine grid indexes as the reference solution $\phi^{\mathbf{ref}}$. We consider the initial conditions and parameters setting as Eq. (36). To compute the convergence rate for the temporal discretization with the fixed $h = 1/512$, we choose the set of decreasing time steps as $\Delta t = 3.2\text{e}-4$, $\Delta t = 1.6\text{e}-4$ and $\Delta t = 8\text{e}-5$. The reference solution is assumed to be

Table 1
Errors and convergence rates with different time steps for velocity field u and v, phase field ϕ and temperature field T.

Δt	Error				Order			
	u	v	ϕ	T	u	v	ϕ	T
3.2e − 4	6.638e − 02	1.621e − 03	1.216e − 02	4.075e − 02	–	–	–	–
1.6e − 4	1.508e − 02	3.389e − 04	3.102e − 03	9.297e − 03	2.14	2.25	1.97	2.13
8e − 5	3.532e − 03	8.586e − 05	7.821e − 04	2.444e − 03	2.09	1.98	1.99	1.93

Table 2
Errors and convergence rates with different space steps for velocity field u and v, phase field ϕ and temperature field T.

N	Error				Order			
	u	v	ϕ	T	u	v	ϕ	T
64	2.465e − 03	2.623e − 04	9.258e − 04	7.312e − 03	–	–	–	–
128	6.554e − 04	6.912e − 05	2.205e − 04	1.808e − 03	1.91	1.94	2.07	2.02
256	1.345e − 04	1.808e − 05	5.131e − 05	4.171e − 04	2.28	1.94	2.10	2.12

obtained of temporal step $\Delta t = 2\mathrm{e}-5$. Here, the error is defined as $e_{i,\Delta t} := \phi_{i,\Delta t} - \phi_i^{\mathbf{ref}}$. Let $\log_2(\|e_{i,\Delta t}\|_2/\|e_{i,\Delta t/2}\|_2)$ be the rate of convergence. The errors and the rates of the convergence have been presented in Table 1. As can be seen, the proposed method is indeed second-order accuracy in time, which is expected from the discrete scheme Eq. (20).

To demonstrate the convergence rate for the spatial discretization with the fixed temporal step size $\Delta t = 2\mathrm{e}-5$ until $t = 0.1$, we use the set of decreasing spatial steps as $h = 1/64$, $h = 1/128$ and $h = 1/256$. Here, the error is defined as $e_{i,h} := \phi_{i,h} - \phi_i^{\mathbf{ref}}$. Let $\log_2(\|e_{i,h}\|_2/\|e_{i,h/2}\|_2)$ be the rate of convergence. The reference solution is assumed to be obtained with a very fine space grid size $h = 1/512$. The results are shown in Table 2. As can be seen from the results, our method is indeed second-order accuracy with respect to space.

Comparing to the direct solution of the optimization problem, the benefits of our proposed method should be remarked here: (i) Our algorithm is second-order accurate, which implies that our method uses fewer iterative steps than the general direct optimization algorithm. (ii) Our algorithm can ensure the energy dissipation law, which means that it will not fall into local extreme points and get pseudo convergence.

4.3. Presentation of various classical shape optimization problems

In this subsection, we demonstrate several classical cases, such as the personalized design of the diffuser, growing evolution of the pip bend and the arterial bypass design. The initial conditions are set as

$$\phi_1(x,y,0) = \begin{cases} 1, & \text{if } x = 0 \text{ and } 10/3 \le y \le 20/3, \\ 1, & \text{if } x = 10 \text{ and } 10/3 \le y \le 20/3, \\ \text{rand}(x,y), & \text{otherwise}, \end{cases} \qquad \phi_2(x,y,0) = \begin{cases} 1, & \text{if } x = 0 \text{ and } 7 \le y \le 9, \\ 1, & \text{if } x = 10 \text{ and } 1 \le y \le 3, \\ \text{rand}(x,y), & \text{otherwise}, \end{cases}$$

$$\phi_3(x,y,0) = \begin{cases} 1, & \text{if } y = 0 \text{ and } 1 \le x \le 3, \\ 1, & \text{if } y = 0 \text{ and } 7 \le x \le 9, \\ \text{rand}(x,y), & \text{otherwise}. \end{cases}$$

The initial velocity field for the three examples are chosen as

$$\mathbf{u}_1(x,y,0) = \begin{cases} (0.5y(10-y),0), & \text{if } x = 0 \text{ and } 10/3 \le y \le 20/3, \\ (6.75(y-10/3)(20/3-y),0), & \text{if } x = 10 \text{ and } 10/3 \le y \le 20/3, \\ (0,0), & \text{otherwise}, \end{cases}$$

$$\mathbf{u}_2(x,y,0) = \begin{cases} ((y-7)(9-y),0), & \text{if } x = 0 \text{ and } 7 \le y \le 9, \\ ((y-1)(3-y),0), & \text{if } x = 10 \text{ and } 1 \le y \le 3, \\ (0,0), & \text{otherwise}, \end{cases}$$

$$\mathbf{u}_3(x,y,0) = \begin{cases} (0,(x-1)(3-x)), & \text{if } y = 0 \text{ and } 1 \le x \le 3, \\ (0,(x-7)(x-9)), & \text{if } y = 0 \text{ and } 7 \le x \le 9, \\ (0,0), & \text{otherwise}. \end{cases}$$

The initial temperature of the three examples are chosen as

$$T_1(x,y,0) = \text{rand}(x,y), \quad T_2(x,y,0) = \text{rand}(x,y), \quad T_3(x,y,0) = \text{rand}(x,y),$$

where $\text{rand}(x,y)$ is a random number between 0 and 1. In our computations, the prescribed volume fraction for the three examples are chosen as $V_0 = 50$. The top row is the schematic illustration of inflow and outflow, the middle row is

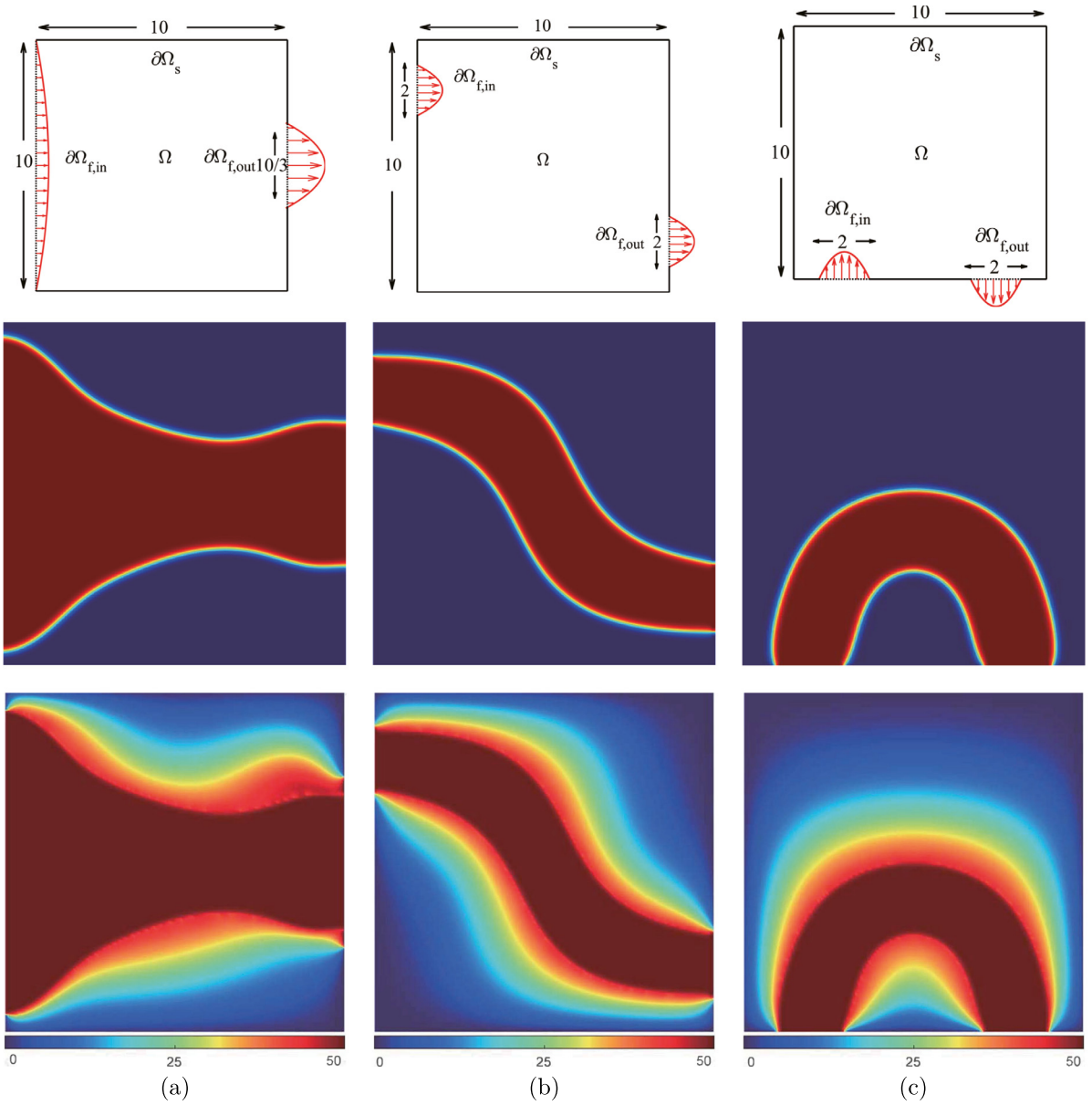

Fig. 2. Three classical shape optimization problems. (a) is the diffuser design, (b) is the curved pip design and (c) is the arterial bypass design. The top row is the illustration of the initial conditions, the middle row is the results of the phase-field evolution and the bottom row is the temperature field by the proposed method.

the phase-field results of topology optimization and the bottom row is the temperature field of the three examples. To show the temperature changes resulting from the optimization, we assume that the temperature of the fluid is constant and the heat is continuously diffused outward. From Fig. 2(a) to 2(c), the sub-figures show the results of the diffuser, pipe and bypass, respectively. According to these results, it can be seen that the fluid flow drives the deformation of the boundary between the fluid domain and the solid domain, thus the optimized shape is finally formed under the interaction between the fluid and the solid. The bottom row shows the results of heat diffusion with the thermal-fluid of constant temperature. As can be seen from the results in Fig. 3, the evolution of the objective results dissipate. It is worth pointing out that the final optimization result is independent on the initial condition of the phase field. In other words, we can set an initial value condition that is approximate to the optimized target shape to shorten the iterative process and accelerate convergence.

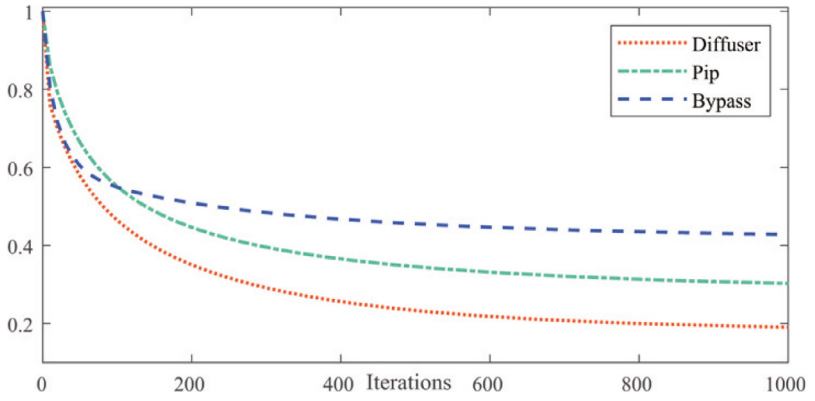

Fig. 3. Energy dissipation of the three classical shape optimization problems, i.e., diffuser, pip and bypass.

4.4. Comparing the influence of the volume fractions

In this section, we perform a comparison test to demonstrate the influence of the volume fraction for topology optimization. We assume that the inlet is at the top of the box and the outlet is on the other three sides. We choose the initial phase field as $\phi(x, y, 0) = \text{rand}(x, y)$, the temperature field as $T(x, y, 0) = \text{rand}(x, y)$ and the initial velocity field as:

$$\mathbf{u}(x, y, 0) = \begin{cases} (0, (x-4.5)(x-5.5)), & \text{if } y = 0, \quad 4.5 \le x \le 5.5, \\ (0, (x-3.5)(x-6.5)), & \text{if } y = 10, \quad 3.5 \le x \le 6.5, \\ ((4.5-y)(y-5.5), 0), & \text{if } x = 0, \quad 4.5 \le y \le 5.5, \\ ((y-4.5)(y-5.5), 0), & \text{if } x = 10, \quad 4.5 \le y \le 5.5, \\ (0, 0), & \text{otherwise.} \end{cases}$$

For the velocity field $\mathbf{u}$ and phase field ϕ, we apply the Dirichlet boundary condition, i.e., the inlet and outlet fluid velocity is consistent with the initial velocity field and the opening size remains the same during the evolution. It can be seen from Fig. 4, under the constraint of the initial velocity and the volume fraction, the topological structures has been characterized. By comparing the results obtained with different volume fraction, i.e. $V_0 = 50$ and 60, the following properties can be summarized: (i) The topological shape is influenced by the volume fraction of the fluid domain as well as the position of inlet and outlet and initial velocity field. (ii) The small volume fraction results in a solid domain in the middle of the fluid domain and the lid-driven flow in the square cavity can be obtained during the evolution. (iii) The large volume fraction results in the uniform fluxes for the three outlets. Furthermore, we have to conclude that the volume fraction can influence the velocity field during the evolution and leads to different topological structures.

4.5. Topology optimization in an arbitrary domain

We will apply a topology optimization test in an arbitrary domain to verify that the proposed method is not limited by the computational domain. To show the efficiency of the proposed system, we consider the computational domain as $\Omega = [0, 10] \times [0, 10]$ with a 512×512 mesh grid. Here we use the Dirichlet boundary conditions for the blank domain and assume that the temperature in the blank area is constant, i.e. $\phi(x, y, t) = 0$ and $T(x, y, t) = T_0$, if $(x, y) \in \partial\Omega_s$. The heat source is located in the black domain and provides thermal energy for the whole system. The initial conditions are chosen as

$$\phi(x, y, 0) = \begin{cases} \text{rand}(x, y), & \text{if } (x, y) \in \Omega \backslash \Omega_s, \\ 0, & \text{otherwise,} \end{cases}$$

$$\mathbf{u}(x, y, 0) = \begin{cases} (0, (x-4.5)(x-5.5)), & \text{if } y = 0, \quad 4.5 \le x \le 5.5, \\ (0, (x-4.5)(x-5.5)), & \text{if } y = 10, \quad 4.5 \le x \le 5.5, \\ ((4.5-y)(y-5.5), 0), & \text{if } x = 0, \quad 4.5 \le y \le 5.5, \\ ((y-4.5)(y-5.5), 0), & \text{if } x = 10, \quad 4.5 \le y \le 5.5, \\ (0, 0), & \text{otherwise,} \end{cases}$$

$$T(x, y, 0) = \begin{cases} T_0, & \text{if } (x, y) \in \Omega_s, \\ 0, & \text{otherwise.} \end{cases}$$

The schematic illustration is shown in Fig. 5. The other non-default parameters are chosen as: $K_1 : K_2 = 10 : 10$, $C_1 : C_2 = 200 : 200$, $\mu_1 : \mu_2 = 0.1 : 0.1$, $\tilde{\alpha}_\epsilon = 10$, $\gamma = 0.1$ and $T_0 = 10$. Since the initial state is with random contributions,

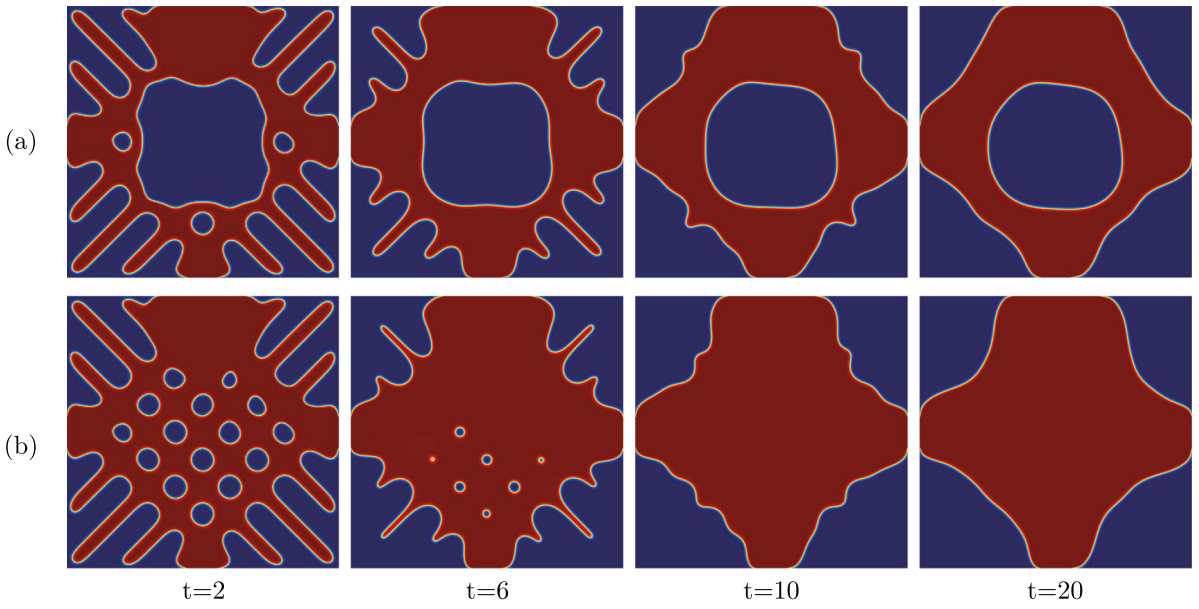

Fig. 4. The dynamical behaviors of phase-field with different volume fraction (a) V_0=50 and (b) V_0=60. From left to right, the indicate times are t = 2, 6, 10 and 20, respectively.

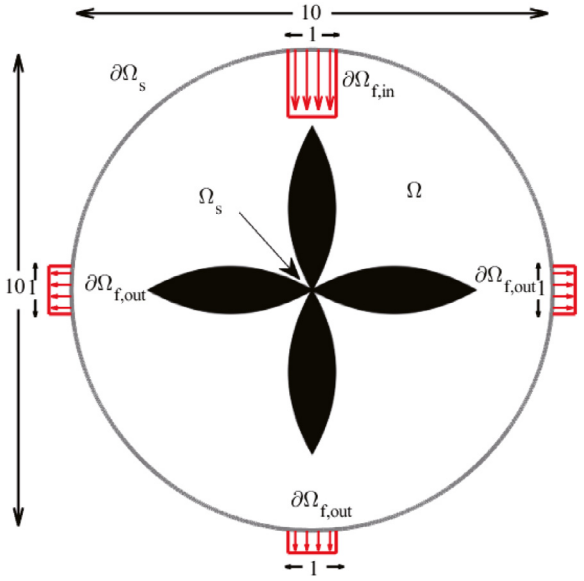

Fig. 5. Schematic illustration of the initial velocity field and the computational domain.

we will perform a long-time evolution to simulate the changes of the topological structure and temperature. Fig. 6(a) and (b) are the evolution of the phase-field and the temperature field. The indicated times for capturing are t = 0, 4, 8 and 20, respectively. From Fig. 6(a) we can see that the phase field converges under the influence of the fluid velocity field and gradually forms a rhomboid pipe. From Fig. 6(b), we can see that the heat is spreading out from the center along the fixed solid region, the temperature field has gradually evolved into a well-distributed mode from the initial distribution, which corresponds with the physical context. Furthermore, we demonstrate the original energy and the modified energy with or without heat source in Fig. 7. Since the heat source brings heat into the system, the total energy of the system increases. Meanwhile, the modified energy and the original energy without heat source are non-increasing.

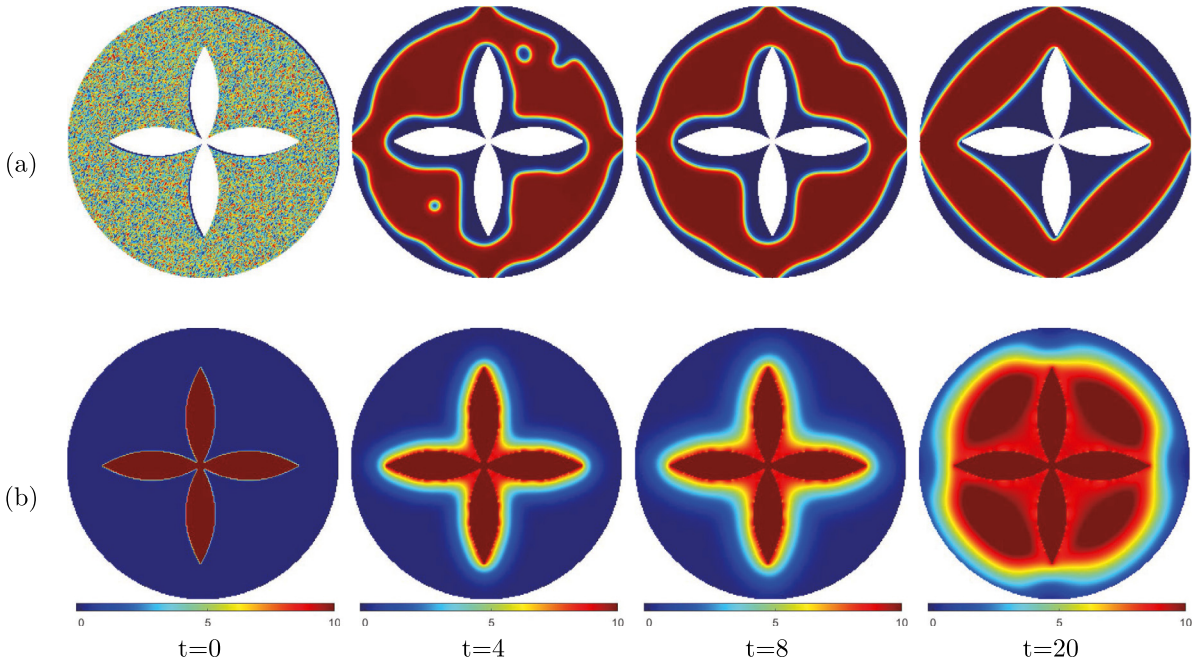

Fig. 6. The dynamical behaviors of the topology optimization procedure in an complex domain. (a) is the evolution of the phase-field and (b) is the evolution of the temperature field. From left to right, the indicated times are t = 0, 4, 8 and 20, respectively.

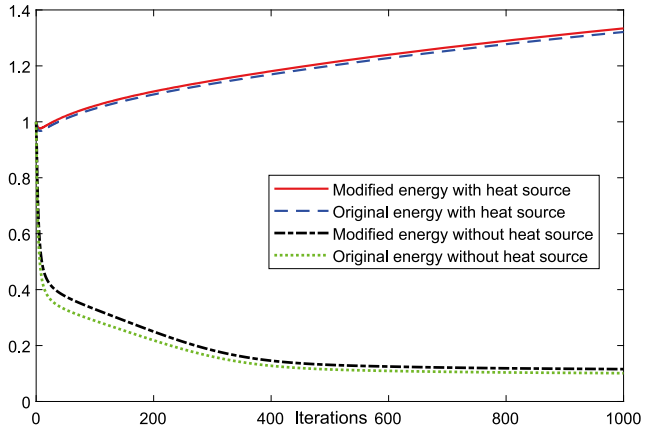

Fig. 7. The evolution of the modified energy and the original energy with or without heat source.

4.6. Investigation of the influence on the dynamics depending on time step

In this subsection, we will investigate the influence on the dynamics on time step to demonstrate the effectiveness of the proposed method. The initial conditions are chosen as:

$$\phi(x,y,0) = \mathrm{rand}(x,y)\left(0.5 - 0.5\tanh\left(\frac{1.5-\sqrt{(x-5)^2+(y-5)^2}}{\sqrt{2}\epsilon}\right)\right),$$

$$\mathbf{u}(x,y,0) = \begin{cases} ((y-7)(9-y),0), & \text{if } x = 0 \text{ or } 10, \quad 7 \le y \le 9, \\ (0,0), & \text{otherwise}, \end{cases}$$

$$T(x,y,0) = \mathrm{rand}(x,y).$$

The other non-default parameters are chosen as $\mu_1 : \mu_1 = 0.01 : 0.01$, $\beta = 1$, $V_0 = 70$ and $\gamma = 0.1$. As shown in Fig. 8, the results are obtained, from left to right, with time step $\Delta t = h$, $0.1h$ and $0.01h$, respectively. Obviously, it can be seen that there is no visible difference between the results obtained by using the time step of $0.1h$ and $0.01h$, while the results

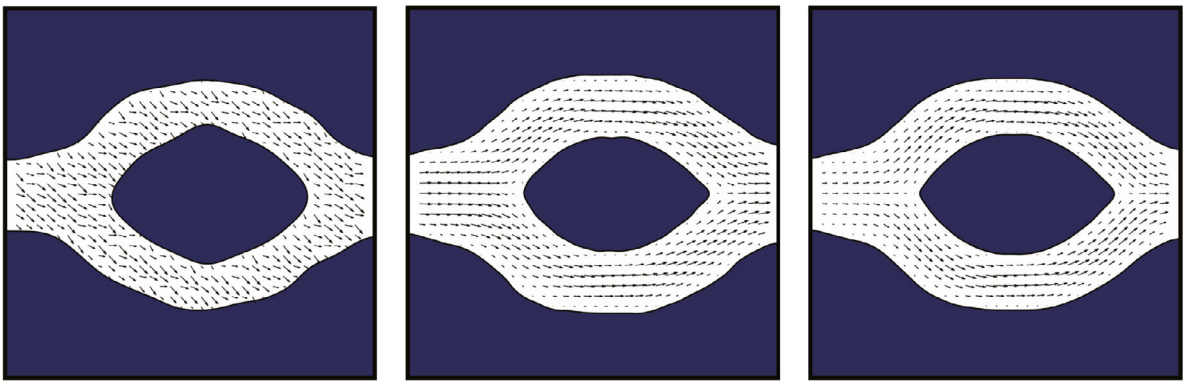

Fig. 8. The results of the dynamics velocity field with different time step. From left to right, the result is obtained with $\Delta t = h$, $0.1h$ and $0.01h$, respectively.

obtained by using $\Delta t = h$ are disordered. Considering the strong coupling relation of the optimization problem, the time step $\Delta t = 0.1h$ is efficient. In addition, we need to emphasize that the value of ϵ should not be too large, otherwise pseudo diffusion results will be obtained under the influence of mean curvature caused by the phase field function Eq. (10). The value of ϵ should not be too small, otherwise computation will be interrupted due to the sharp interface.

4.7. Comparison with previous method

We will perform the numerical tests to compare the topological changes with previous method [65]. They used a level-set method to track shapes and the deformations by combining the Hadamard's method and the body-fitted approach. In this subsection, we compare the results with the simulation of [65]. In order to maximize heat removal through fluid flow, we need to revise the modified objective function and add a convective term as:

$$\begin{aligned}\min_{\Omega} J(\phi, \mathbf{u}, T) = &\int_{\Omega} \left(\frac{\mu}{2}|\nabla \mathbf{u}|^2 - \mathbf{u}\cdot\mathbf{f}\right)\, \mathrm{d}\mathbf{x} + \gamma \int_{\Omega} \left(\frac{\epsilon}{2}|\nabla\phi|^2 + \frac{1}{\epsilon}F(\phi)\right)\, \mathrm{d}\mathbf{x} \\ &+ \int_{\Omega} \frac{\alpha(\phi)}{2}|\mathbf{u}|^2\, \mathrm{d}\mathbf{x} + \int_{\Omega} \frac{1}{2}T^2\, \mathrm{d}\mathbf{x} + \frac{\beta}{2}\left(\int_{\Omega}\phi\, \mathrm{d}\mathbf{x} - V_0\right)^2 - \int_{\Omega} \rho C_p \mathbf{u}\cdot\nabla T\, \mathrm{d}\mathbf{x},\end{aligned} \tag{41}$$

subject to Eq. (7)–(8). We assume that the fluid flows into the left side with fixed velocity $\mathbf{u}_0$ and T_0 and flows out of the right side. It is worth pointing out that minimizing the last term is equivalent to maximize the heat loss with a fix initial condition of the fluid. We no longer carry out volume restrictions on fluid flux in this numerical test. Therefore, the objective function can be simplified as:

$$\begin{aligned}\min_{\Omega} J(\phi, \mathbf{u}, T) = &\int_{\Omega} \frac{\mu}{2}|\nabla \mathbf{u}|^2\, \mathrm{d}\mathbf{x} + \gamma \int_{\Omega} \left(\frac{\epsilon}{2}|\nabla\phi|^2 + \frac{1}{\epsilon}F(\phi)\right)\, \mathrm{d}\mathbf{x} + \int_{\Omega} \frac{1}{2}T^2\, \mathrm{d}\mathbf{x} \\ &+ \int_{\Omega} \frac{\alpha(\phi)}{2}|\mathbf{u}|^2\, \mathrm{d}\mathbf{x} - \left(\int_{\partial\Omega_{\text{in}}} \rho C_p T_0 \mathbf{u}_0\cdot\mathbf{n}\, \mathrm{d}s + \int_{\partial\Omega_{\text{out}}} \rho C_p T\mathbf{u}\cdot\mathbf{n}\, \mathrm{d}s\right),\end{aligned} \tag{42}$$

where minimizing the last term in Eq. (41) means maximizing the heat flux out, i.e., $\max \int_{\partial\Omega_{\text{out}}} \rho C_p T\mathbf{u}\cdot\mathbf{n}\, \mathrm{d}s$, where $\mathbf{n}$ is the out normal vector toward to $\partial\Omega$. On the upper and lower boundaries, the Neumann boundary condition is used for the velocity field and temperature field and the Dirichlet boundary condition is used for the phase field. Since we use no external forces on the boundary, the divergence free conditions does not rest on the boundary. In addition to the default parameters, we specify that the other parameters are chosen as: $\gamma = 100$, $\mu_1 : \mu_2 = 0.01 : 0.01$, $\Delta t = h^2$, $\beta = 0$ and $\mathbf{f} = (0,\ 0)$. The initial conditions of phase variable ϕ are demonstrated in Fig. 9(a) and the topological results by the proposed method are shown in Fig. 9(b). The white line is the 0-contour line and the color map is corresponding to the norm of the velocity. The closed regions with white lines are considered solid regions(low permeability) in our model. It is obvious that the corresponding complex topology shape in [65] can also be obtained by our method. Furthermore, we have to point out that the energy stability can be conserved by our proposed method.

4.8. Three dimensional test

In this subsection, we applied the topology optimization procedure with diffuser in three dimension as shown in Fig. 10. The computational domain is chosen as $\Omega = [0, 10] \times [0, 10] \times [0, 10]$ with a $128 \times 128 \times 128$ mesh grid. The initial

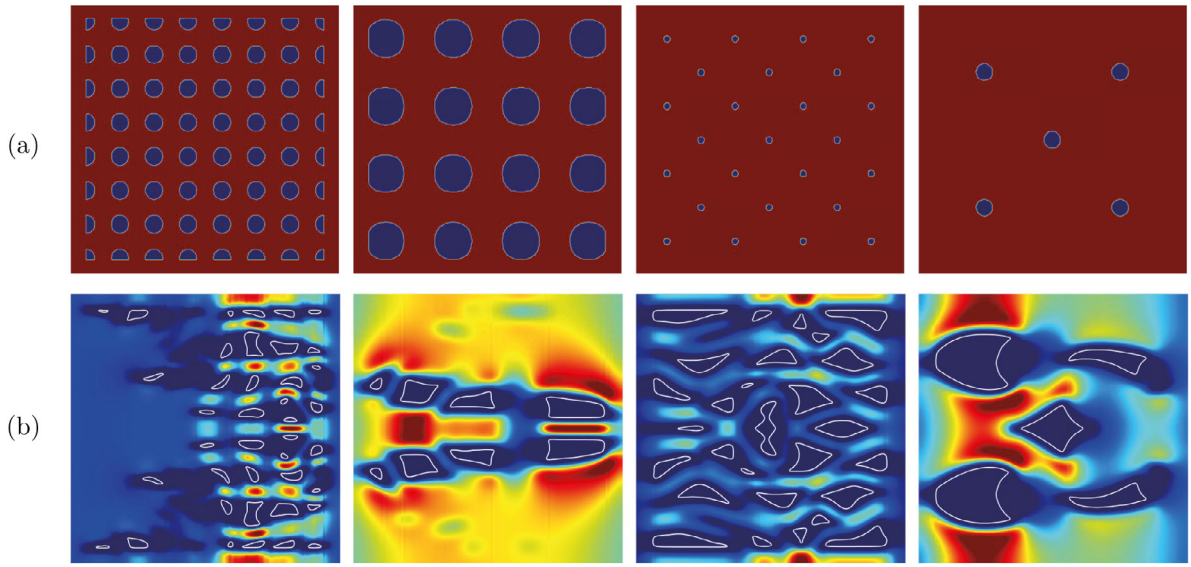

Fig. 9. Topology optimization without volume constraint. (a) Initial condition of phase variable ϕ. (b) The results of by the proposed method.

conditions are chosen as

$$\phi(x,y,z,0) = 0.5\left(1-\tanh\left(\frac{\left((|z-5|-1.5)^2+(|y-5|-1.5)^2-1\right)}{2\sqrt{2}\epsilon}\right)\right),$$

$$\mathbf{u}(x,y,z,0) = \begin{cases} 0.5\left(1-\tanh\left(\dfrac{\left((y-5)^2+(z-5)^2-4^2\right)}{2\sqrt{2}\epsilon}\right)\right), & \text{if } x=0, \\ 0.5\left(1-\tanh\left(\dfrac{\left((|y-5|-1.5)^2+(|z-5|-1.5)^2-1^2\right)}{2\sqrt{2}\epsilon}\right)\right), & \text{if } x=10, \\ (0,0), & \text{otherwise}, \end{cases}$$

$$T(x,y,z,0) = \phi(x,y,z,0).$$

We choose one flow profile on the inflow boundary with center of circles being $(0, 5, 5)$. The radius of the circle is 2. We choose the four flow profile on the outflow boundary with centers of circles being $(10,\ 2.5,\ 2.5)$, $(10,\ 7.5,\ 2.5)$, $(10,\ 2.5,\ 7.5)$ and $(10,\ 7.5,\ 7.5)$, respectively. The radius of all circles equals 1. From Fig. 10(a) to (d), we demonstrate the dynamical behaviors of the topology optimization with diffuser in three dimension at indicated times t = 0, 3, 6 and 10, respectively. It is obvious that the optimal configuration is smooth, which indicates that our method works well for solving the three dimensional optimization problem. Furthermore, we demonstrate the evolution of the non-increasing original energy in the three dimensional domain in Fig. 11. Note that the original energy has been normalized by the initial energy. The inset figures are the slices ($x = 5,\ y = 5,\ z = 5$) of the optimal design results at the indicated times $t = 0$, 3, 6 and 10, respectively. It can be seen from Fig. 11, the original energy reaches a steady state at $t = 5$. The discrete energy in three dimension dissipates, which confirms that the proposed scheme is stable.

5. Conclusion

In this paper, an efficient topology optimization scheme for the thermal fluid was established, which is influenced by several constraints, to adaptively design the fluid–solid coupling structure and force the objective energy dissipate. We used the variational derivation and couple the Stokes equation and the heat transfer equation based on the phase-field model. We have proved the existence of minimal solutions to the optimization problem under the constraints of multiple physical fields. The Crank–Nicolson method was applied to discrete the numerical system. We proved the original energy and the modified energy dissipate in the continuous and discrete framework respectively, which ensured that a larger time step can be used in our method. The proposed discrete system maintains second-order spatial and temporal accuracy. Several numerical tests were demonstrated to indicate that the numerical approach is efficient to design the complicated structures of thermal-fluid flows.

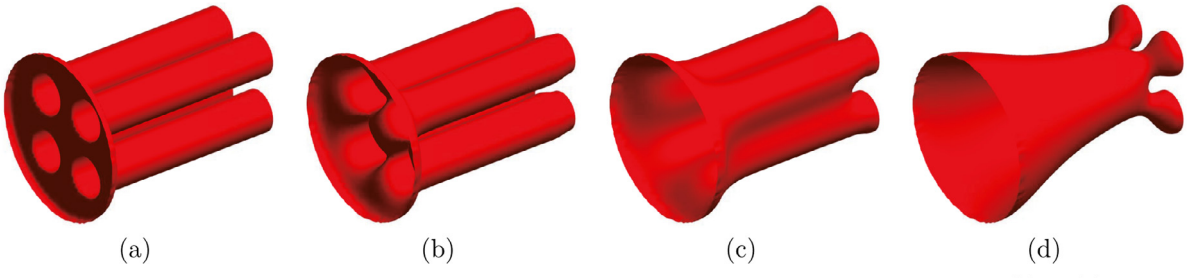

Fig. 10. The dynamical behaviors of the topology optimization with diffuser in three dimension. From (a) to (d) right, the indicated times are t = 0, 3, 6 and 10, respectively.

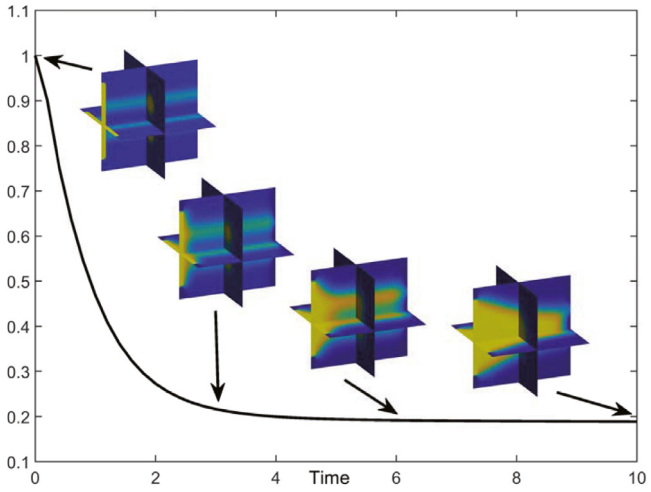

Fig. 11. The evolution of the non-increasing original energy in the three-dimensional simulation. The inset figures are the slices ($x = 5, y = 5, z = 5$) of the optimal design results at the indicated times $t = 0$, 3, 6 and 10, respectively. The original energy has been normalized by the initial energy.

CRediT authorship contribution statement

Qing Xia: Conceptualization, Methodology, Software, Investigation, Visualization, Writing – original draft. **Gangming Sun:** Conceptualization, Writing – review & editing. **Qian Yu:** Conceptualization, Supervision. **Junseok Kim:** Conceptualization, Writing – review & editing, Supervision. **Yibao Li:** Conceptualization, Methodology, Software, Writing – review & editing, Supervision, Project administration.

Declaration of competing interest

The authors declare that they have no known competing financial interests or personal relationships that could have appeared to influence the work reported in this paper.

Data availability

No data was used for the research described in the article.

Acknowledgments

J.S. Kim was supported by Basic Science Research Program through the National Research Foundation of Korea (NRF) funded by the Ministry of Education (NRF-2019R1A2C1003053). Y.B. Li is supported by the Fundamental Research Funds for the Central Universities, China (No. XTR042019005). The authors are grateful to the reviewers whose valuable suggestions and comments significantly improved the quality of this paper.

References

[1] Bendsøe MP, Kikuchi N. Generating optimal topologies in structural design using a homogenization method. Comput Methods Appl Mech Engrg 1988;71:197–224.
[2] Yu Q, Xia Q, Li Y. A phase field-based systematic multiscale topology optimization method for porous structures design. J Comput Phys 2022;466:111383.
[3] Wang MY, Wang X, Guo D. A level set method for structural topology optimization. Comput Methods Appl Mech Engrg 2003;192:227–46.
[4] Eschenauer HA, Othoff N. Topology optimization of continuum structures: A review. Appl Mech Rev 2001;54:331–90.
[5] Li Y, Wang K, Yu Q, Xia Q, Kim J. Unconditionally energy stable schemes for fluid-based topology optimization. Commun Nonlinear Sci 2022;111:106433.
[6] Hazra S. Multigrid one-shot method for aerodynamic shape optimization. SIAM J Sci Comput 2008;30:1527–47.
[7] Muyl F, Dumas L, Herbert V. Hybrid method for aerodynamic shape optimization in automotive industry. Comput Fluids 2004;33:849–58.
[8] Pingen G, Evgrafov A, Maute K. Topology optimization of flow domains using the lattice Boltzmann method. Struct Multidiscipl Optim 2007;34:507–24.
[9] Deng Y, Liu Z, Zhang P, Liu Y, Wu Y. Topology optimization of unsteady incompressible Navier–Stokes flows. J Comput Phys 2011;20:6688–708.
[10] Li Y, Zhu J, Zhang W, Wang L. Structural topology optimization for directional deformation behavior design with the orthotropic artificial weak element method. Struct Multidiscip Optim 2018;57:1251–66.
[11] Zhang H, Luo Y, Kang Z. Bi-material microstructural design of chiral auxetic metamaterials using topology optimization. Compos Struct 2018;195:232–48.
[12] Subramaniama V, Dbouk T, Hariona JL. Topology optimization of conjugate heat transfer systems: A competition between heat transfer enhancement and pressure drop reduction. Int J Heat Fluid Flow 2019;75:165–84.
[13] Bunker RS. Gas turbine heat transfer ten remaining hot gas path challenges. J Turbomach 2007;129:1–14.
[14] Koga AA, Lopes ECC, Villa Nova HF, d. Lima CR, Silva ECN. Development of heat sink device by using topology optimization. Int J Heat Mass Transfer 2013;64:759–72.
[15] Haertel JHK, Nellis GF. A fully developed flow thermofluid model for topology optimization of 3D-printed air-cooled heat exchangers. Appl Therm Eng 2017;119:10–24.
[16] Li Y, Xia Q, Yoon S, Lee C, Lu B, Kim J. Simple and efficient volume merging method for triply periodic minimal structures. 264, 2021, 107956.
[17] Borrvall T, Petersson J. Topology optimization of uids in Stokes flow. Internat J Numer Methods Fluids 2003;41:77–107.
[18] Gersborg-Hansen A, Sigmund O, Haber R. Topology optimization of channel flow problems. Struct Multidiscip Optim 2005;30:181–92.
[19] Xia Q, Kim J, Li Y. Modeling and simulation of multi-component immiscible flows based on a modified Cahn-Hilliard equation. Eur J Mech B-Fluid 2022;95:194–204.
[20] Hao Y, Huang Q, Wang C. A third order BDF energy stable linear scheme for the No-Slope-Selection thin film model. Commun Comput Phys 2021;29:905–29.
[21] Olesen LH, Okkels F, Bruus H. A high-level programming–language implementation of topology optimization applied to steady–state Navier–Stokes flow. Int J Numer Methods Engrg 2006;65:975–1001.
[22] Othmer C. A continuous adjoint formulation for the computation of topological and surface sensitivities of ducted flows. Internat J Numer Methods Fluids 2008;58:861–77.
[23] Kubo S, Yaji K, Yamada T, Izui K, Nishiwaki S. A level set–based topology optimization method for optimal manifold designs with flow uniformity in plate–type microchannel reactors. Struct Multidiscip Optim 2017;55:1311–27.
[24] Romero JS, Silvab ECN. A topology optimization approach applied to laminar flow machine rotor design. Comput Methods Appl Mech Engrg 2014;279:268–300.
[25] Dirker J, Meyer JP. Topology optimization for an internal heat-conduction cooling scheme in a square domain for high heat flux applications. J Heat Transfer 2013;135:111010.
[26] Marck G, Nemer M, Harion JL, Russeil S, Bougeard D. Topology optimization using the simp method for multiobjective conductive problems. Numer Heat Transf B 2012;61:439–70.
[27] Bruns TE. Topology optimization of convection-dominated, steady-state heat transfer problems. Int J Heat Mass Transfer 2007;50:2859–73.
[28] Iga A, Nishiwaki S, Izui K, Yoshimura M. Topology optimization for thermal conductors considering design-dependent effects, including heat conduction and convection. Int J Heat Mass Transfer 2009;52:2721–32.
[29] Hassani B, Hinton E. A review of homogenization and topology optimization I–homogenization theory for media with periodic structure. Comput Struct 1998;69:707–17.
[30] Sigmund O, Clausen PM. Topology optimization using a mixed formulation: An alternative way to solve pressure load problems. Comput Methods Appl Mech Engrg 2007;196:1874–89.
[31] Aage N, Poulsen TH, Gersborg-Hansen A, Sigmund O. Topology optimization of large scale Stokes flow problems. Struct Multidiscip Optim 2008;35:175–80.
[32] Papoutsis-Kiachagias EM, Giannakoglou KC. Continuous adjoint methods for turbulent flows, applied to shape and topology optimization: industrial applications. Arch Comput Methods Eng 2016;23:255–99.
[33] Yoon GH. Topology optimization for stationary fluid–structure interaction problems using a new monolithic formulation. Int J Numer Math Engng 2010;82:591–616.
[34] Vicente WM, Picelli R, Pavanello R, Xie YM. Topology optimization of frequency responses of fluid–structure interaction systems. Finite Elem Anal Des 2015;98:1–13.
[35] Xia Q, Yu Q, Li Y. A second-order accurate, unconditionally energy stable numerical scheme for binary fluid flows on arbitrarily curved surfaces. Comput Methods Appl Mech Engrg 2021;384:113987.
[36] Feppon F, Allaire G, Dapogny C, Jolivet P. Body–fitted topology optimization of 2D and 3D fluid–to–fluid heat exchangers. Comput Methods Appl Mech Engrg 2021;376:113638.
[37] Daróczy L, Jármai K. From a quasi-static fluid-based evolutionary topology optimization to a generalization of BESO. Eng Optim 2015;47:689–705.
[38] Sokolowski J, Zochowski A. On the topological derivative in shape optimization. SIAM J Control Optim 1999;37:1251–72.
[39] Suresh K. Efficient generation of large–scale pareto–optimal topologies. Struct Multidiscipl Optim 2013;47:49–61.
[40] Sá LFN, Amigo RCR, Novotny AA, Silva ECN. Topological derivatives applied to fluid flow channel design optimization problems. Struct Multidiscip Optim 2016;54:249–64.
[41] Challis VJ, Guest JK. Level set topology optimization of fluids in Stokes flow. Internat J Numer Methods Engrg 2009;79:1284–308.
[42] Kreissl S, Maute K. Levelset based fluid topology optimization using the extended finite element method. Struct Multidiscip Optim 2012;46:311–26.
[43] Sethian JA, Wiegmann A. Structural boundary design via level set and immersed interface methods. J Comput Phys 2000;163:489–528.
[44] Li Y, Xia Q, Lee C, Kim S, Kim J. A robust and efficient fingerprint image restoration method based on a phase-field model. Pattern Recognit 2022;123:108405.

[45] Li Y, Liu R, Xia Q, He C, Li Z. First- and second-order unconditionally stable direct discretization methods for multi-component Cahn–Hilliard system on surfaces. J Comput Appl Math 2022;401:113778.
[46] Garcke H, Hecht C, Hinze M, Kahle C. Numerical approximation of phase field based shape and topology optimization for fluids. SIAM J Sci Comput 2015;37:A1846–71.
[47] Blank L, Garcke H, Hecht C, Rupprecht C. Sharp interface limit for a phase field model in structural optimization. SIAM J Control Optim 2016;54:1558–84.
[48] Garcke H, Hecht C. Shape and topology optimization in Stokes flow with a phase field approach. Appl Math Opt 2016;73:23–70.
[49] Deng Y, Liu Z, Wu Y. Topology optimization of capillary, two–phase flow problems. Commun Comput Phys 2017;22:2017.
[50] Li F, Yang J. A provably efficient monotonic-decreasing algorithm for shape optimization in stokes flows by phase–field approaches. SIAM J Numer Anal 2021. arXiv preprint arXiv:2107.09260.
[51] Liu C, Wang C, Wang Y, Wise SM. Convergence analysis of the variational operator splitting scheme for a reaction–diffusion system with detailed balance. SIAM J Numer Anal 2022;60:781–803.
[52] Wang C, Wise SM. An energy stable and convergent finite-difference scheme for the modified phase field crystal equation. SIAM J Numer Anal 2011;49:945–69.
[53] Diegel AE, Wang C, Wang X, Wise SM. Convergence analysis and error estimates for a second order accurate finite element method for the Cahn-Hilliard-Navier–Stokes system. Numer Math 2017;137:495–534.
[54] Garcke H, Hecht C. A phase field approach for shape and topology optimization in Stokes flow. New Trends Shape Optim 2015;103–15.
[55] Schmid A. A time dependent Ginzburg–Landau equation and its application to the problem of resistivity in the mixed state. Phys Kondens Mater 1966;5:302–17.
[56] Modica L. The gradient theory of phase transitions and the minimal interface criterion. Arch Ration Mech Anal 1987;98:123–42.
[57] Chen H, Wang X. A one-domain approach for modeling and simulation of free fluid over a porous medium. J Comput Phys 2014;259:650–71.
[58] Temam R. Navier–Stokes equations: theory and numerical analysis. vol. 343, American Mathematical Soc.; 2001.
[59] Hu Z, Wise SM, Wang C, Lowengrub JS. Stable and efficient finite-difference nonlinear-multigrid schemes for the phase field crystal equation. J Comput Phys 2009;228:5323–39.
[60] Zhu G, Chen H, Li A, Sun S, Yao J. Fully discrete energy stable scheme for a phase-field moving contact line model with variable densities and viscosities. Appl Math Model 2020;83:614–39.
[61] Du Q, Ju L, Li X, Qiao Z. Maximum principle preserving exponential time differencing schemes for the nonlocal Allen–Cahn equation. SIAM J Numer Anal 2019;57:875–98.
[62] Shen J, Tang T, Yang J. On the maximum principle preserving schemes for the generalized Allen–Cahn equation. Commun Math Sci 2016;14:1517–34.
[63] Témam R. Sur l'approximation de la solution des équations de Navier–Stokes par la méthode des pas fractionnaires II. Arch Ration Mech Anal 1969;33:377–85.
[64] Lozada-Cruz G. Some variants of Cauchy's mean value theorem. J Sci Educ Technol 2020;51:1155–63.
[65] Feppon F, Allaire G, Dapogny C, Jolivet P. Body-fitted topology optimization of 2D and 3D fluid–to–fluid heat exchangers. Comput Methods Appl Mech Engrg 2021;376:113638.